Geophysical Journal International

Geophys. J. Int. (2022) **229,** 1212–1231
Advance Access publication 2022 January 04
GJI Seismology

https://doi.org/10.1093/gji/ggab529

3-D synthetic modelling and observations of anisotropy effects on SS precursors: implications for mantle deformation in the transition zone

Quancheng Huang,[1,2] Nicholas C. Schmerr,[1] Caroline Beghein,[3] Lauren Waszek[4,2] and Ross R. Maguire[1,5]

[1] *Department of Geology, University of Maryland, College Park, MD* 20742, *USA. E-mail: qchuang@umd.edu*
[2] *Department of Physics, New Mexico State University, Las Cruces, NM* 88003, *USA*
[3] *Department of Earth, Planetary, and Space Sciences, University of California, Los Angeles, CA* 90095, *USA*
[4] *Physical Sciences, James Cook University, Townsville, QLD* 4811, *Australia*
[5] *Department of Earth and Planetary Sciences, University of New Mexico, Albuquerque, NM* 87131, *USA*

Accepted 2022 January 2. Received 2021 November 20; in original form 2021 May 17

SUMMARY

The Earth's mantle transition zone (MTZ) plays a key role in the thermal and compositional interactions between the upper and lower mantle. Seismic anisotropy provides useful information about mantle deformation and dynamics across the MTZ. However, seismic anisotropy in the MTZ is difficult to constrain from surface wave or shear wave splitting measurements. Here, we investigate the sensitivity to anisotropy of a body wave method, SS precursors, through 3-D synthetic modelling and apply it to real data. Our study shows that the SS precursors can distinguish the anisotropy originating from three depths: shallow upper mantle (80–220 km), deep upper mantle above 410 km, and MTZ (410–660 km). Synthetic resolution tests indicate that SS precursors can resolve $\geq$3 per cent azimuthal anisotropy where data have an average signal-to-noise ratio (SNR $=$ 7) and sufficient azimuthal coverage. To investigate regional sensitivity, we apply the stacking and inversion methods to two densely sampled areas: the Japan subduction zone and a central Pacific region around the Hawaiian hotspot. We find evidence for significant V_S anisotropy (15.3 $\pm$ 9.2 per cent) with a trench-perpendicular fast direction ($93^\circ \pm 5^\circ$) in the MTZ near the Japan subduction zone. We attribute the azimuthal anisotropy to the grain-scale shape-preferred orientation of basaltic materials induced by the shear deformation within the subducting slab beneath NE China. In the central Pacific study region, there is a non-detection of MTZ anisotropy, although modelling suggests the data coverage should allow us to resolve at least 3 per cent anisotropy. Therefore, the Hawaiian mantle plume has not produced detectable azimuthal anisotropy in the MTZ.

Key words: Composition and structure of the mantle; Numerical modelling; Body waves; Seismic anisotropy; Hotspots; Subduction zone processes.

1 INTRODUCTION

Convection in Earth's mantle is strongly influenced by the properties of the mantle transition zone (MTZ), a distinct layer that controls the thermal and compositional exchange between the upper and lower mantle (Morgan & Shearer 1993; Bercovici & Karato 2003). The boundary of the MTZ is defined by two sharp seismic discontinuities at 410-km and 660-km depths. The formation of these discontinuities is a consequence of the pressure-induced phase changes of the upper mantle mineral olivine. Mineral physics experiments show that the phase change of olivine to wadsleyite occurs at 410-km depth, and the dissociation of ringwoodite to bridgmanite + ferropericlase occurs at 660-km depth (Ringwood 1975; Ita & Stixrude 1992). The opposite Clapeyron slopes of the olivine phase changes (Ito & Takahashi 1989; Katsura & Ito 1989) make them useful for studying the mantle thermal and compositional heterogeneities (Bina & Helffrich 1994; Stixrude 1997; Helffrich 2000) via mapping of MTZ topography (Flanagan & Shearer 1998).

The SS precursors are seismic body waves that manifest as shear wave reflections occurring at the underside of the 410-km and 660-km discontinuities (Fig. 1). They have served as a primary tool to investigate topography on these discontinuities at both regional (e.g. Thomas & Billen 2009; Schmerr *et al*. 2010; Yu *et al*. 2017) and

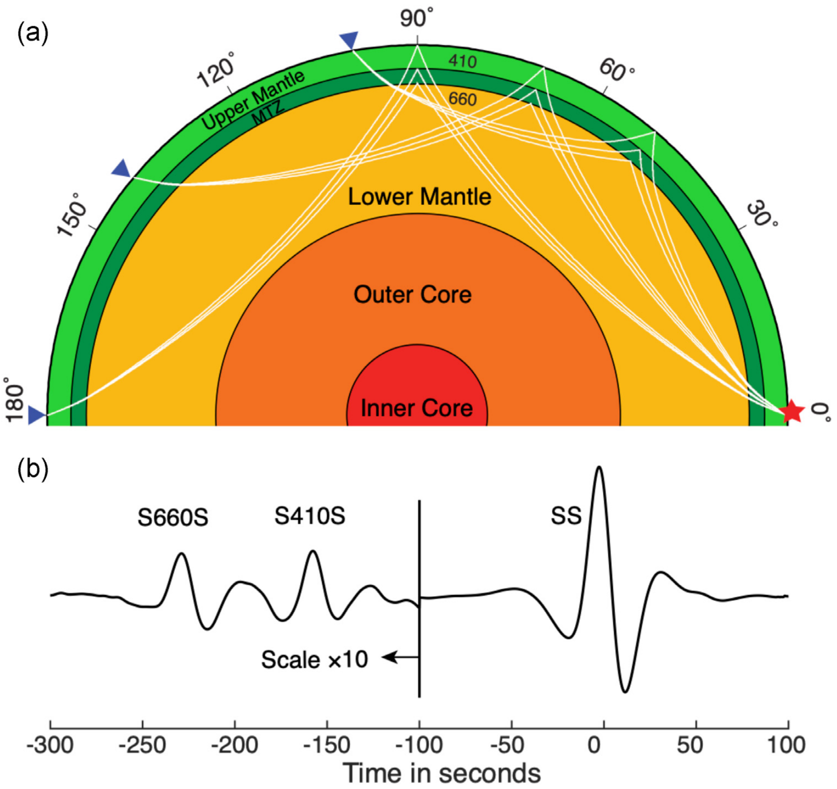

Figure 1. (a) Ray paths of SS phase and SS precursors at the epicentral distances of 100°, 140° and 180°. The red star and blue triangles represent the source and receivers, respectively. (b) An example of stacked waveform of SS phase and SS precursors. The amplitudes of S410S and S660S are amplified by 10 times to facilitate comparisons with the SS phase.

global scales (e.g. Flanagan & Shearer 1998; Deuss & Woodhouse 2002; Gu & Dziewonski 2002; Houser *et al*. 2008; Lawrence & Shearer 2008; Huang *et al*. 2019; Guo & Zhou 2020). The SS precursors that reflect from the 410-km and 660-km discontinuities are named as S410S and S660S, respectively, or generally referred to as SdS where ‘d’ is the depth of discontinuity within the Earth. Several studies of the SS precursors have detected seismic anisotropy in the upper mantle and MTZ (Rychert *et al*. 2012, 2014; Huang *et al*. 2019). Seismic anisotropy, the dependence of seismic velocity on propagation direction and polarization, is a useful tool to constrain mantle deformation and dynamics. It is primarily produced by two key mechanisms: the lattice-preferred orientation (LPO) of intrinsically anisotropic minerals under a dislocation creep regime, or the shape-preferred orientation (SPO) of isotropic materials with distinct elastic properties (e.g. due to compositional layering or lenses of melt). Here we further evaluate the sensitivity of the SS precursors to mantle anisotropy, to assess the extent to which these seismic phases can provide insights into mantle deformation and dynamics in the MTZ.

Observations of upper mantle anisotropy are traditionally obtained from shear wave splitting (e.g. Silver & Chan 1988; Long & van der Hilst 2005; Marone & Romanowicz 2007), surface wave dispersion (e.g. Anderson 1962; Montagner & Nataf 1986; Nettles & Dziewoński 2008) and global tomography models (e.g. Gung *et al*. 2003; Moulik & Ekström 2014; Chang *et al*. 2015). Anisotropy in the uppermost ∼250 km of the mantle is typically interpreted as the LPO of olivine (Karato *et al*. 2008) caused by the current pattern of mantle flow in the asthenosphere or the preservation of paleo-flow directions in the lithosphere (i.e. ‘fossil anisotropy’). In the deep upper mantle above 410 km, the observed seismic anisotropy is generally lower with amplitudes ≤1 per cent (Yuan & Beghein 2013, 2018; Auer *et al*. 2014; Chang *et al*. 2014) and the relation between fast seismic direction and deformation is less straightforward than at shallower depths (Mainprice *et al*. 2005). At MTZ depths, evidence for seismic anisotropy is more limited, but consistently reported from multiple methods: shear wave splitting (Tong *et al*. 1994; Fouch & Fischer 1996; Chen & Brudzinski 2003; Foley & Long 2011), surface wave measurements (Trampert & van Heijst 2002; Yuan & Beghein 2013, 2014, 2018; Debayle *et al*. 2016), coupling of normal modes (Beghein *et al*. 2008), *P*-to-*S* converted phases (Zhang *et al*. 2021) and inversion of deep earthquake focal mechanisms (Li *et al*. 2018). The surface wave models that incorporate higher mode surface waves (Yuan & Beghein 2013, 2014; Debayle *et al*. 2016; Schaeffer *et al*. 2016) suggest that ∼1–2 per cent azimuthal anisotropy exists in the MTZ globally, despite regional discrepancies amongst these models. Recently, Ferreira *et al*. (2019) found ubiquitous radial anisotropy in the MTZ and uppermost lower mantle in the vicinity of western Pacific subduction zones. Our previous study using SS precursors (Huang *et al*. 2019) also presented regional evidence for 3 per cent azimuthal anisotropy in the MTZ beneath subduction zones but detected negligible anisotropy (<1 per cent) at a global scale.

Unlike the upper mantle, where deformation is expressed as the LPO of the mineral olivine, the MTZ may have several possible mechanisms for accommodating seismic anisotropy. For example, the MTZ anisotropy in subduction zones has primarily been attributed to the LPO of wadsleyite (Kawazoe *et al*. 2013), although the SPO of subducting slabs has also been proposed (Faccenda *et al*. 2019). In the upper transition zone (410–520 km), wadsleyite has up to ∼14 per cent single-crystal V_S anisotropy (Sawamoto *et al*. 1984; Zha *et al*. 1997; Sinogeikin *et al*. 1998), making wadsleyite the main candidate mineral for accommodating anisotropy at these depths. Below 520 km, ringwoodite is nearly isotropic with a cubic structure (Weidner *et al*. 1984; Kiefer *et al*. 1997; Sinogeikin *et al*. 2003; Li *et al*. 2006). Other minerals such as majorite garnet and clinopyroxene have either weak single-crystal anisotropy, or not enough mineral fraction abundance to accommodate the seismic observations of MTZ anisotropy (Bass & Kanzaki 1990; Sang & Bass 2014; Pamato *et al*. 2016). Slab mineralogy and layering may provide an alternative mechanism for accommodating anisotropy in the deep transition zone (Faccenda *et al*. 2019). Although wadsleyite can accommodate up to 14 per cent anisotropy, it must be aligned by mantle dynamics into a fabric detectable by seismic waves. Numerical simulations of strain-induced fabric of mantle mineral aggregates are therefore key to understanding the relationship between mantle flow direction (or strength) and fast direction (or strength) of seismic anisotropy in the MTZ. Previous modelling has primarily focused on the upper mantle anisotropy (Becker 2006), whereas few studies explore deeper anisotropy in the MTZ and uppermost lower mantle (Faccenda 2014; Sturgeon *et al*. 2019). For example, Sturgeon *et al*. (2019) predicts that up to ∼2 per cent V_S radial anisotropy may form in the MTZ beneath subduction zones. Mineral physics modelling by Tommasi *et al*. (2004) predicts that ∼1 per cent V_S azimuthal anisotropy can exist within the MTZ.

Although the sensitivities of SS precursors to the topography of 410-km and 660-km discontinuities have been investigated (Zhao & Chevrot 2003; Bai *et al*. 2012; Koroni & Trampert 2016), their sensitivities to azimuthal anisotropy at MTZ depths remain unexplored. Motivated by both geodynamic and mineral physics predictions, we use SS precursors to better constrain anisotropy at MTZ depths, thereby illuminating the dynamics of the upper mantle. In this study, we construct 3-D models of anisotropy and propagate synthetic seismic waves through the models to test the sensitivity of SS precursors to azimuthal anisotropy. We next compare the results of our modelling to observations in the central Pacific region and Japan subduction zone to determine the detectability and sensitivity of the SS precursory phases to MTZ anisotropy. Finally, we interpret mantle deformation in the MTZ in the context of our observations.

2 METHODS

2.1 SS data set

We expanded a global hand-picked SS data set described in Huang *et al*. (2019) and Waszek *et al*. (2018) to include large earthquakes ($M_w \geq 6.0$) from 1988 to 2017 in the depth range 0–75 km (previously only 0–30 km) recorded at broadband stations with epicentral distances between 100° and 180°. The signal-to-noise ratio (SNR) was computed from the amplitude of SS phase over the maximum amplitude in a noise window (65–275 s before SS phase. Records with SNR lower than 2.5 were removed from the data set. The final SS data set consists of 58 566 seismograms. We used the transverse component of the data to study the azimuthal anisotropy. To remove seismic noise, we filtered the data between 15 and 50 s using a Butterworth bandpass filter and aligned the waveform at the peak amplitude of the SS phase. Each SS seismogram was then normalized to unity to equalize the SS arrivals across events and stations.

2.2 3-D synthetics

We used the spectral element code SPECFEM3D_GLOBE (Komatitsch & Tromp 2002a,b) to compute 3-D synthetic SS precursor waveforms. The mesh consisted of six domains with 320 spectral elements on each side. Therefore, the minimum resolvable period of the synthetics was 13.6 s. We turned on attenuation, Earth's rotation and gravity for the simulations, and turned off the ellipticity, topography, and ocean flags to implement a 1-D crust model. We created 13 earthquakes around the target region and synthesized a dense array to provide ideal azimuthal coverage (Figs 2 and 3). The focal mechanism of each earthquake was designed to maximize the SH energy in the receiver direction. We set the half duration of the Gaussian source-time function to be 10 s. The length of each seismogram was set to be one hour, and they were rotated to radial and transverse components automatically. Each simulation took ∼4 hr by using 384 CPUs on a High Performance Computing (HPC) cluster. After computing the synthetics, we generated random noise based on the realistic power spectrum of Earth's noise (Peterson 1993) and added it to the synthetics. The synthetics were then processed in the same way as the data which was described in Section 2.1.

We chose two study regions that are densely sampled by the SS phase: (1) the central Pacific region near Hawaii (Fig. 2) and (2) the Japan subduction zone (Fig. 3). The goal was to simulate the azimuthal anisotropy generated by a mantle plume versus a subducting slab. In each region, we created two types of source–receiver geometries: idealized and realistic geometry. The idealized geometry provided at least 100 records in each 15° azimuthal bin to ensure enough data for the stacking of SS precursors. The realistic geometry was a subset of the idealized geometry designed to mimic the actual azimuthal coverage of the data that sample each region. This anisotropic structure was introduced over the Preliminary Reference Earth Model (PREM, Dziewonski & Anderson 1981) at three depth ranges: (1) the shallow upper mantle (80–220 km); (2) the deep upper mantle (250–400 km) and (3) the MTZ (400–670 km). The boundaries of these layers coincide with the discontinuities in PREM such as 220-, 400- and 670-km discontinuities. The models at each depth included three strengths of anisotropy: 1, 3 and 5 per cent. The input fast directions were due north (0°) in the central Pacific bin and trench perpendicular (270°) in the Japan bin. The models outside the target depth ranges (e.g. crust and lower mantle) kept the 1-D PREM structures. We set the radius of the central Pacific bin to 10° (∼1100 km) and the size of the Japan bin to 1500 × 1000 km. The choice in size of the central Pacific structure was controlled by the standard deviation of normal distribution, and we explored the effects of lateral size of anisotropic structures on resolution using 5° and 2.5° radius.

2.3 Stacking and corrections

The SS precursors are typically similar in amplitude to background noise or less, thus their retrieval requires stacking when noise is present. Here, we followed the stacking methods of Schmerr & Garnero (2006) to stack the precursors along the predicted traveltime curves from PREM. We chose 125° as our reference distance, and applied moveout corrections to align the SS precursors on the predicted traveltime at the reference distance using PREM. We also applied distance exclusion windows (0°–100° and 135°–145° for S410S; 0°–115° and 165°–180° for S660S) to avoid interferences with topside reflections (e.g. Sv660sS) and ScS reverberations (e.g. ScS^660ScS). We stacked the data by azimuth of the ray path at

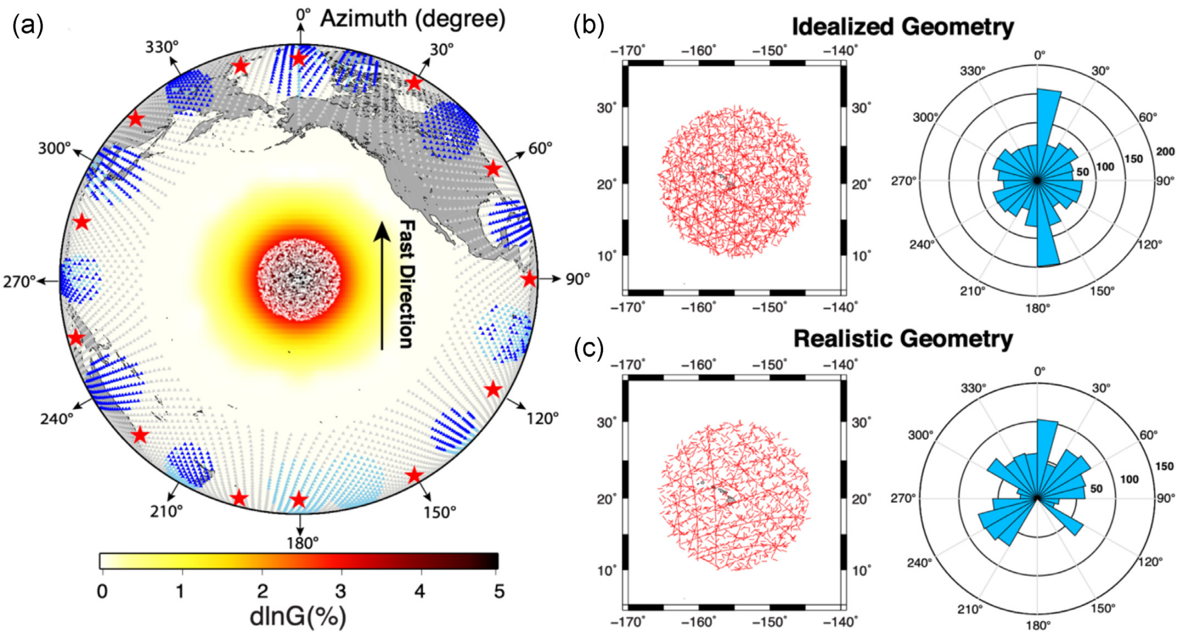

Figure 2. (a) Source–receiver geometry for the model in the central Pacific region. The red stars denote the earthquake sources. The input fast direction is due north (0°). The triangles represent all the stations: the light blue + dark blue stations are the ones used for the idealized geometry; the dark blue stations only are the ones used for the realistic geometry; the grey stations are the unused ones. The white points in the centre are the SS bounce points with a bin radius of 10° (∼1100 km). (b) The SS bounce points in the idealized geometry (left-hand panel) and their azimuthal distribution (right-hand panel). The orientations of the red sticks (left-hand panel) represent the azimuths of the SS bounce points. (c) The SS bounce points in the realistic geometry (left-hand panel) and the azimuthal distribution of the bounce points (right-hand panel) which mimics the azimuthal coverage of data in this region.

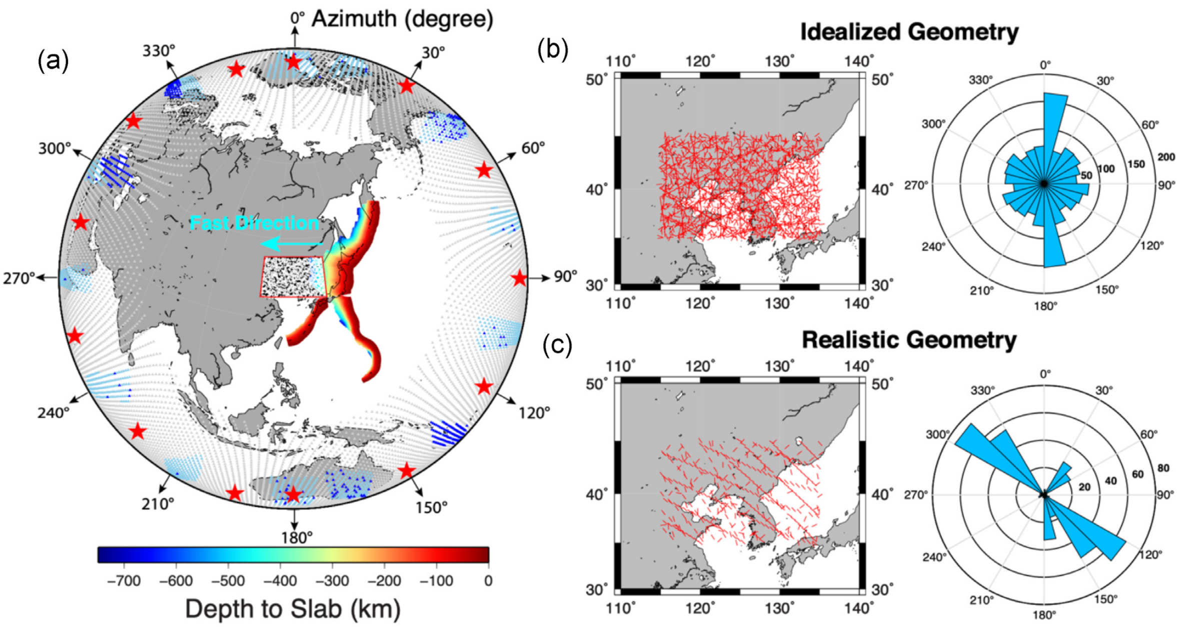

Figure 3. (a) Source–receiver geometry for the model in the Japan subduction zone. The source, receiver and bounce point legends are the same as Fig. 2. The study region is highlighted by the red box and the size is 1500 km × 1000 km. The strength of anisotropy is a uniform value thus represented in black colour and the fast direction is trench-perpendicular (270°). The values of slab depths are from Slab 1.0 model (Hayes *et al*. 2012). (b) The SS bounce points in the idealized geometry (left-hand panel) and their azimuthal distribution (right-hand panel). The orientations of the red sticks (left-hand panel) represent the azimuths of the SS bounce points. (c) The SS bounce points in the realistic geometry (left-hand panel) and their azimuthal distribution (right-hand panel).

the central bounce-point of SS to study the azimuthal variations of SS precursor traveltimes and amplitudes. The 2σ uncertainties of traveltime and amplitude measurements were estimated from a bootstrapping technique that implemented 300 resamples, allowing replacements within each bin (Efron & Tibshirani 1986).

We applied a series of traveltime and amplitude corrections to ensure that precursor traveltimes and amplitudes were not contaminated by factors other than anisotropy, and then inverted for azimuthal anisotropy. Full details regarding traveltime and amplitude correction methods are contained in Huang *et al*. (2019).

(1) The traveltimes of SS precursors are affected by the lateral heterogeneities of crustal and upper mantle structures. We used the CRUST 2.0 model (Bassin *et al*. 2000) for the crustal corrections and the S40RTS model (Ritsema *et al*. 2011) for the tomography corrections. We computed traveltime residuals with respect to PREM based on 1-D ray tracing as pre-stacking traveltime corrections for each individual record. However, global tomography models such as S40RTS tend to average structures across a large region and likely underestimate the V_S anomalies associated with the slab. Therefore, we used a regional tomography model, EARA2014 (Chen *et al*. 2015), in the Japan subduction zone to correct for the sharper and stronger V_S anomalies caused by the subducting slab. (2) We also corrected for the traveltime perturbations caused by topography of 410-km and 660-km discontinuities using the MTZ topography measurements by Huang *et al*. (2019). We computed the topography corrections based on the differences between the local S410S−SS times, S660S−SS times and their global mean values. The S410S−SS and S660S−SS times were measured from the global stacking results after crust and tomography corrections. (3) The amplitudes of SS precursors were corrected for attenuation, geometrical spreading, and focusing and defocusing effects using the 1-D synthetics generated by GEMINI code (Friederich & Dalkolmo 1995). We calculated the amplitude ratios between the stacking results of data and corresponding 1-D synthetics and multiplied by the amplitudes at the reference distance (125°) to remove these effects on amplitudes. The observed data were corrected for both traveltimes and amplitudes, but the 3-D SPECFEM synthetics were only corrected for amplitudes.

2.4 Inversion for azimuthal anisotropy

After applying the amplitude and traveltime corrections, we inverted for the strength and fast direction of azimuthal anisotropy from SdS traveltimes and amplitudes. Here, we consider azimuthal anisotropy as transverse isotropy with a horizontal symmetry axis (Fig. 4a). Therefore, in an anisotropic medium, we can express the velocity of vertically propagating SH wave as the following equations (Crampin 1984; Montagner & Nataf 1986):

$$\rho V_{qSH}^2 = L - G_c \cos 2\psi - G_s \sin 2\psi, \tag{1}$$

$$L = \rho V_{SV}^2 = \frac{1}{2}\left(C_{44} + C_{55}\right), \tag{2}$$

where V_{qSH} is the quasi-SH wave velocity, ρ is density, ψ represents the azimuth of wave propagation direction, L is a combination of elastic coefficients C_{ij}, and G_c and G_s are the azimuthal terms of L (Montagner *et al*. 2000). We can derive the strength of anisotropy (G) and fast direction (Θ) from the G_c and G_s parameters:

$$G = \sqrt{G_s^2 + G_c^2}, \tag{3}$$

$$\Theta = \frac{1}{2}\arctan\left(\frac{G_s}{G_c}\right). \tag{4}$$

Here, we define $dlnG = G/L$ as the relative perturbations of azimuthal anisotropy (Yuan & Beghein 2018). In our inversion, we first built models with a homogeneous layer of anisotropy at three depth ranges as described in Section 2.2. Then, we computed the SdS traveltimes and amplitudes as a function of azimuth (ψ) using SH velocities expressed in eqs (1) and (2). Finally, we used a grid-search method to find the best-fitting G_c and G_s values and used eqs (3) and (4) to compute the fast direction (Θ) and strength of anisotropy (G). During the grid-search process, we calculated the chi-squared values using the following equation:

$$\chi^2 = \sum_{i=1}^{N} \frac{\left(t_i^{\mathrm{obs}} - t_i^{\mathrm{pre}}\right)^2}{\sigma_i^2}, \tag{5}$$

where t_i^{obs} is the observed traveltime of SS precursors, t_i^{pre} is the predicted traveltime, σ_i is the standard deviation of t_i^{obs}, N is the total number of azimuthal bins. The uncertainties of the best-fitting model were estimated from the chi-squared statistics using p-values for two standard deviations.

3 RESULTS

We first investigated the effects of depth, strength and size of anisotropy on measurement resolution using clean synthetics (i.e. no noise) in the central Pacific region. Next, we examined the data in the central Pacific region and Japan subduction zone from which we inverted for azimuthal anisotropy and quantified the uncertainties. Finally, we added realistic noise to the 3-D synthetics for direct comparison to the data, and we also explored the effect of source–receiver geometry on the resolutions.

3.1 Effects of depth, strength and size of anisotropy

Unlike shear wave splitting measurements, SS precursors can distinguish the depths of anisotropy structures based on the combinations of five differential traveltime and amplitude ratio measurements: S410S−SS time, S660S−SS time, S660S−S410S time, S410S/SS and S660S/SS amplitude ratios (Fig. 4). Measurements of SdS differential times are traveltime residuals with respect to the corresponding mean values in each geographical bin. In order to understand the effect of depth, we fixed the size of anisotropic region to be 10° in radius and varied in depth extent. We then performed the synthetic tests described below.

Test (1): Shallow Upper Mantle, Fixed Size. The first experiment simulates anisotropy in the asthenosphere (80–220 km), which is often attributed to the LPO of olivine (Fig. 4a). The SS traveltimes are sensitive to the asthenospheric anisotropy and their variations are mapped to S410S−SS (Fig. 4b) and S660S−SS traveltimes (Fig. 4c) since SS is our reference phase. The S660S−S410S time (Fig. 4d) and amplitudes (Fig. 4e) remain constant because their ray paths do not encounter the anisotropic layer.

Test (2): Deep Upper Mantle, Fixed Size. The second case creates the scenario where anisotropy is only present in the deep upper mantle (250–400 km, Fig. 5a), which can still be caused by the fabric of olivine (Mainprice *et al*. 2005; Mondal & Long 2020). In this model, the S410S/SS amplitude starts to vary with azimuth due to the change of reflection coefficients at 410-km (Fig. 5e), whereas the S660S−S410S time (Fig. 5d) and S660S/SS amplitudes (Fig. 5e) remain constant.

Test (3): MTZ Anisotropy, Fixed Size. The third scenario models an anisotropic layer in the MTZ where the LPO of wadsleyite and ringwoodite are formed (Fig. 6a). The S660S−S410S time becomes an independent measurement for MTZ anisotropy (Fig. 6d) which is not affected by the upper mantle anisotropy. This model includes anisotropy throughout the whole MTZ so both S410S/SS and S660S/SS amplitudes (Fig. 6e) display variations with azimuth. These two amplitudes have opposite trends because the MTZ anisotropy is below the 410-km but above the 660-km discontinuity, thereby changing the signs of reflection coefficients.

Test (4): Two Layers of Anisotropy, Fixed Size. In reality, seismic anisotropy is likely to exist at multiple depths. We combined test

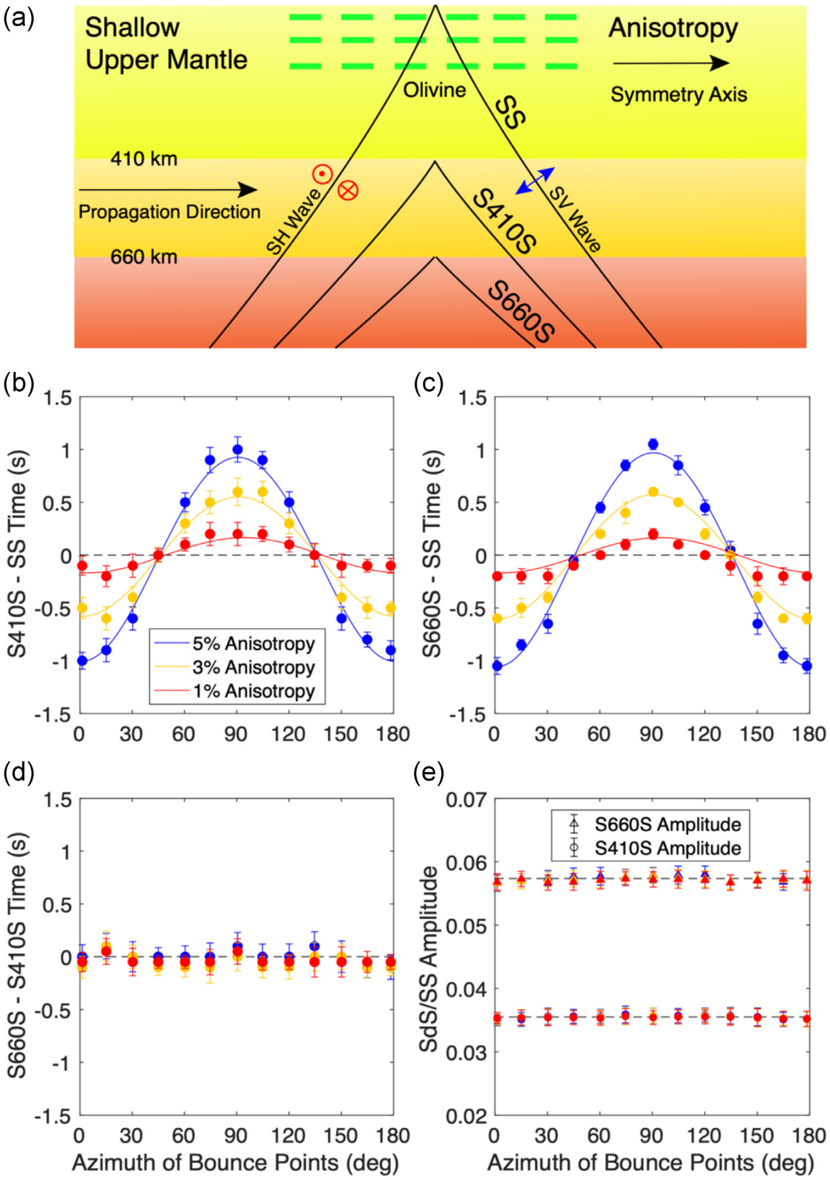

Figure 4. (a) The anisotropy model in the shallow upper mantle (80–220 km). The green bars represent the LPO of olivine. The black curves are the ray paths of SS precursors beneath the bounce point region. The black arrows denote the symmetry axis of azimuthal anisotropy and wave propagation direction. The red and blue arrows show the polarization directions of SH and SV waves, respectively. The measurements of (b) S410S−SS time residuals, (c) S660−SS time residuals, (d) S660S−S410S time residuals, (e) S410S/SS and S660S/SS amplitudes from the azimuthal stacking of SPECFEM3D synthetics are shown as a function of bounce point azimuths. The solid curves are the best-fitting models for 1, 3 and 5 per cent input anisotropy. The dashed lines denote the mean values of each measurement.

(1) and test (3) to create a model with anisotropy existing in both shallow upper mantle and MTZ (Fig. S1a). We rotated the fast axis in the shallow upper mantle (Θ_1) while fixing the fast axis in the MTZ (Θ_2). The goal is to examine the constructive/destructive interferences between upper mantle and MTZ anisotropy. S410S−SS time shows different sinusoidal patterns associated with the change of Θ_1, but the peak-to-peak amplitudes remain the same (Fig. S1b). S660S−SS time transitions from constructive interference to destructive interference as $\Theta_1 - \Theta_2$ increases from 0° to 90° (Fig. S1c). On the contrary, S660S−S410S time (Fig. S1d) and SdS amplitudes (Fig. S1e) are unaffected by the changes in upper mantle anisotropy. This further demonstrates that we can use these measurements to detect MTZ anisotropy unambiguously without contaminations from upper mantle anisotropy. We also tested the effect of two sublayers existing in the upper and lower MTZ (Fig. S2a). In this case, we fixed the fast axis (Θ_2) in the lower MTZ while changing the fast axis (Θ_1) in the upper MTZ. S660S−S410S time starts to exhibit destructive interference as $\Theta_1 - \Theta_2$ increases to 90° (Fig. S2d). The S660S−S410S time can only constrain the bulk structure of MTZ anisotropy, so this measurement alone cannot distinguish two sublayers of anisotropy within the MTZ. However, SdS amplitudes can provide further constraints on the depth of anisotropy if the structures are located near the discontinuities (Fig. S2e).

Test (5): Fixed Depth in the MTZ, Varied Size. The strength and size of anisotropy control the peak-to-peak amplitudes of SdS traveltime and amplitude variations. In this test, the bin radius was fixed at 10° and the anisotropy layer was in the MTZ. Then, we varied

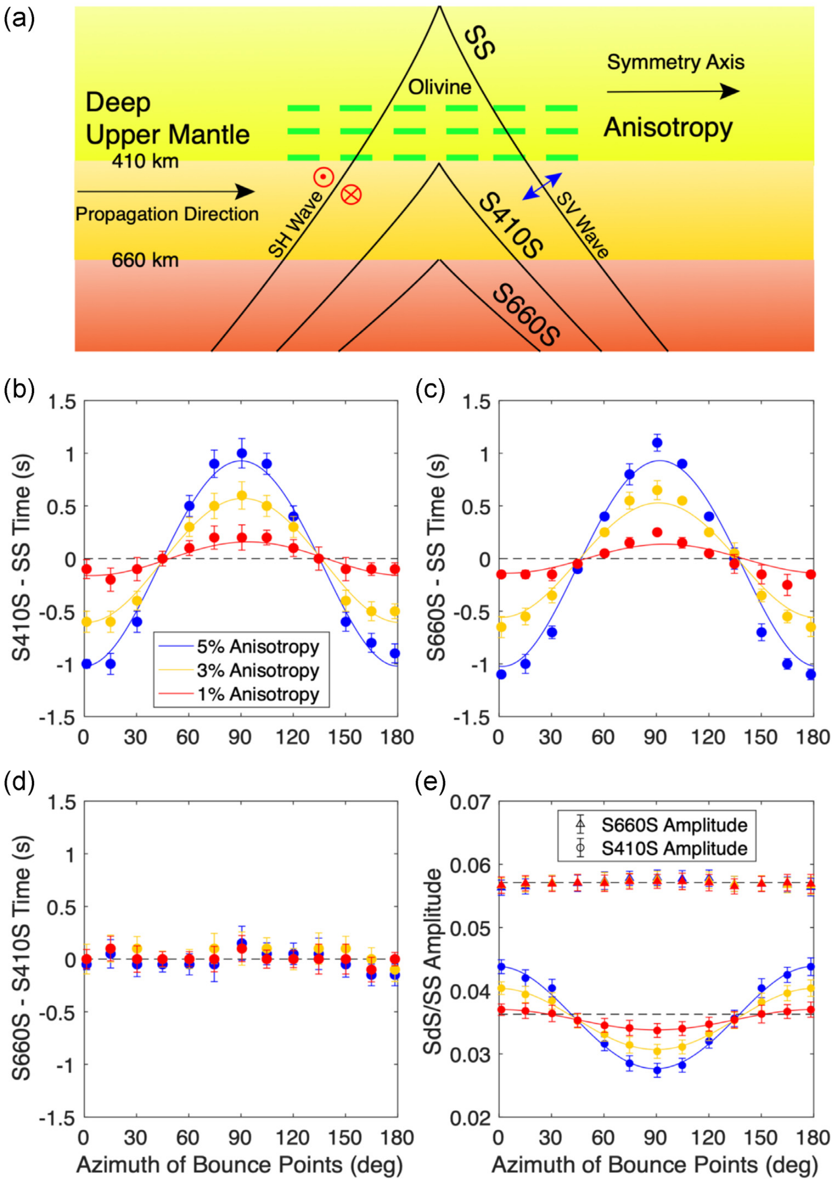

Figure 5. (a) Same as Fig. 4 but for the anisotropy model in the deep upper mantle (250–400 km). The measurements of (b) S410S−SS time residuals, (c) S660S−SS time residuals, (d) S660S−S410S time residuals and (e) S410S/SS and S660S/SS amplitudes from the azimuthal stacking of SPECFEM3D synthetics are shown as a function of bounce point azimuths.

the strength and size of anisotropy and identified four measurements that were sensitive to MTZ anisotropy: S660S−SS time (Fig. 7a), S660S−S410S time (Fig. 7b), S410S/SS and S660S/SS amplitude (Fig. 7c).

The first column of Fig. 7 shows that 3–5 per cent MTZ anisotropy with 10° radius can translate into 0.9–1.5 s traveltime variations, respectively. Generally, the variations caused by anisotropy need to be greater than the corresponding uncertainties of SdS traveltimes or amplitudes to become detectable. The amplitudes of uncertainties are directly related to the noise level in the data or synthetics. We estimated the average 2 σ uncertainties by adding random noise (SNR = 7, the average noise level of our SS data set) to synthetics before stacking (see Section 2.2). The average uncertainties, which are shown as grey shaded regions in Fig. 7, can be used as detection thresholds for SdS traveltimes and amplitudes. When the radius is 10°, Fig. 7 illustrates that the S660S−SS and S660S−S410S times can both detect ≥3 per cent anisotropy. The uncertainties of SdS amplitudes are generally larger in terms of percentage so anisotropy is more difficult to detect, requiring over 5 per cent anisotropy to be detectable. Moving from left to right in Fig. 7, the peak-to-peak amplitudes of SdS traveltimes and amplitudes both decrease as the size of the structure is reduced. When the radius is decreased to 5°, the S660S−SS and S660S−S410S times can only detect ≥5 per cent anisotropy, whereas the variations of SdS amplitudes are below the detection thresholds. The 2.5° radius structures are too small to be detected because all the variations become much lower than the detection thresholds.

3.2 Central pacific data and resolution test

Following the depth, strength and size 3-D synthetic tests, we used our modelling to study the detectability of anisotropy for an SS precursor data set sampling the central Pacific region. In Fig. 8(a),

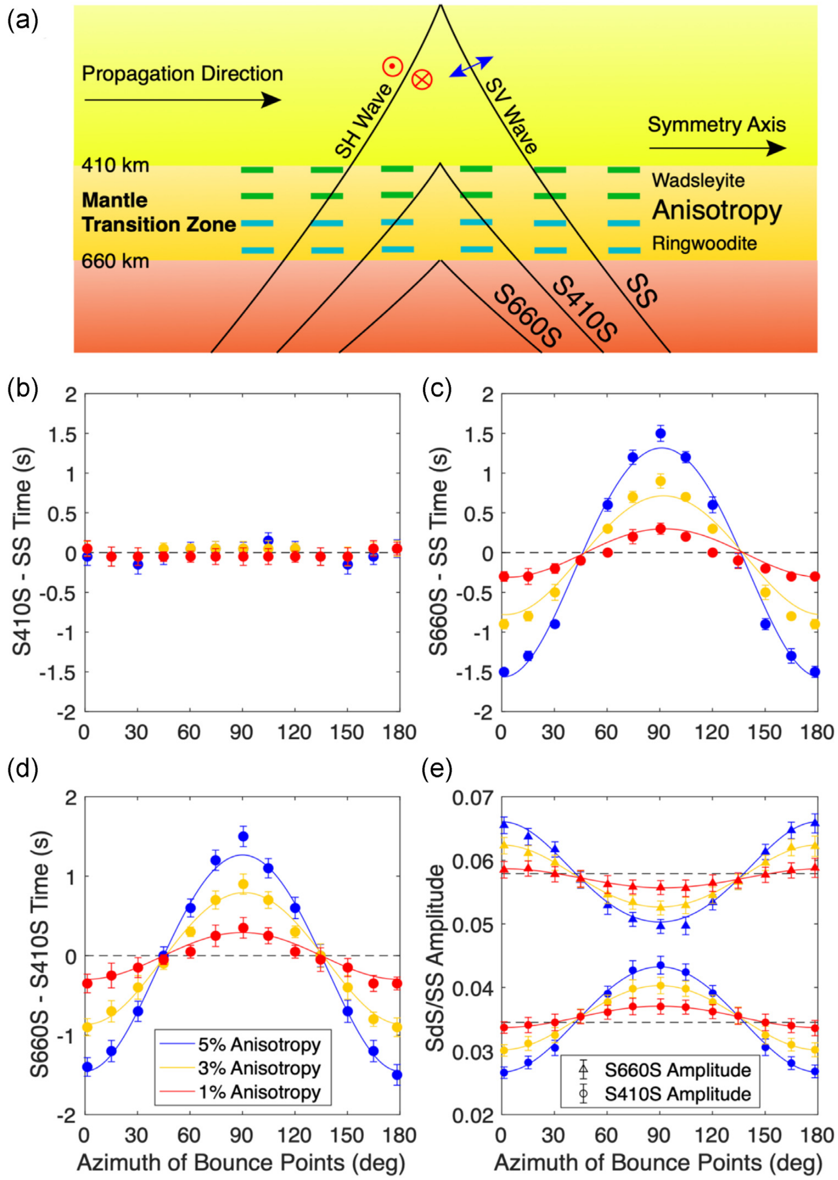

Figure 6. (a) Same as Fig. 4 but for the anisotropy model in the MTZ (400–670 km). The green and blue bars represent the LPO of wadsleyite and ringwoodite, respectively. The measurements of (b) S410S−SS time residuals, (c) S660S−SS time residuals, (d) S660S−S410S time residuals and (e) S410S/SS and S660S/SS amplitudes from the azimuthal stacking of SPECFEM3D synthetics are shown as a function of bounce point azimuths.

the MTZ thickness beneath the central Pacific bin is thinner than average predominantly due to the hot thermal anomalies caused by the Hawaiian hotspot (Schmerr *et al*. 2010). In the S40RTS tomography model (Ritsema *et al*. 2011), the Hawaiian hotspot is associated with slow V_S anomalies in the mantle, which has been interpreted as a mantle plume rising from the core mantle boundary (Fig. 8b). Our goal is to detect signatures of mantle deformation associated with the Hawaiian plume from the constraints on MTZ anisotropy. We divided the data into 30° bins based on the bounce point azimuths. This study region has sufficient azimuthal coverage, and number of records (NR) are greater than 100 in five azimuthal bins (Fig. 8a). Therefore, both S410S and S660S are clearly observed in data (Fig. 8c) and synthetics (Fig. 8d) from azimuthal stacking. We measured the S660S−S410S time residuals and SdS amplitudes from the azimuthally stacked data. The S660S−S410S time residuals for each azimuthal bin are calculated as the traveltime differences between the stacking results of all data in the central Pacific region and the respective bins. We then inverted for azimuthal anisotropy after removing the topography effect on traveltime and applying amplitude corrections as well. Here, we do not consider the S660S−SS and S410S−SS times for anisotropy inversion because they can be contaminated by upper mantle anisotropy.

The best-fitting model for S660S−S410S time indicates that the traveltime variations can be associated with ∼3 per cent MTZ anisotropy in this region (Fig. 9a). However, the chi-squared statistical test suggests that this signal ($\mathrm{dln}G = 2.9 \pm 3.4$ per cent) is not significantly above zero due to the large uncertainty (Fig. 9d). We also performed the inversions for S410S/SS (Fig. 9b) and S660S/SS amplitudes (Fig. 9c) to search for anisotropy near the discontinuities. Anisotropy uncertainties from amplitude inversions (Figs 9e and f) are approximately three times larger than traveltime inversions. Therefore, the anisotropy inverted from amplitudes are not

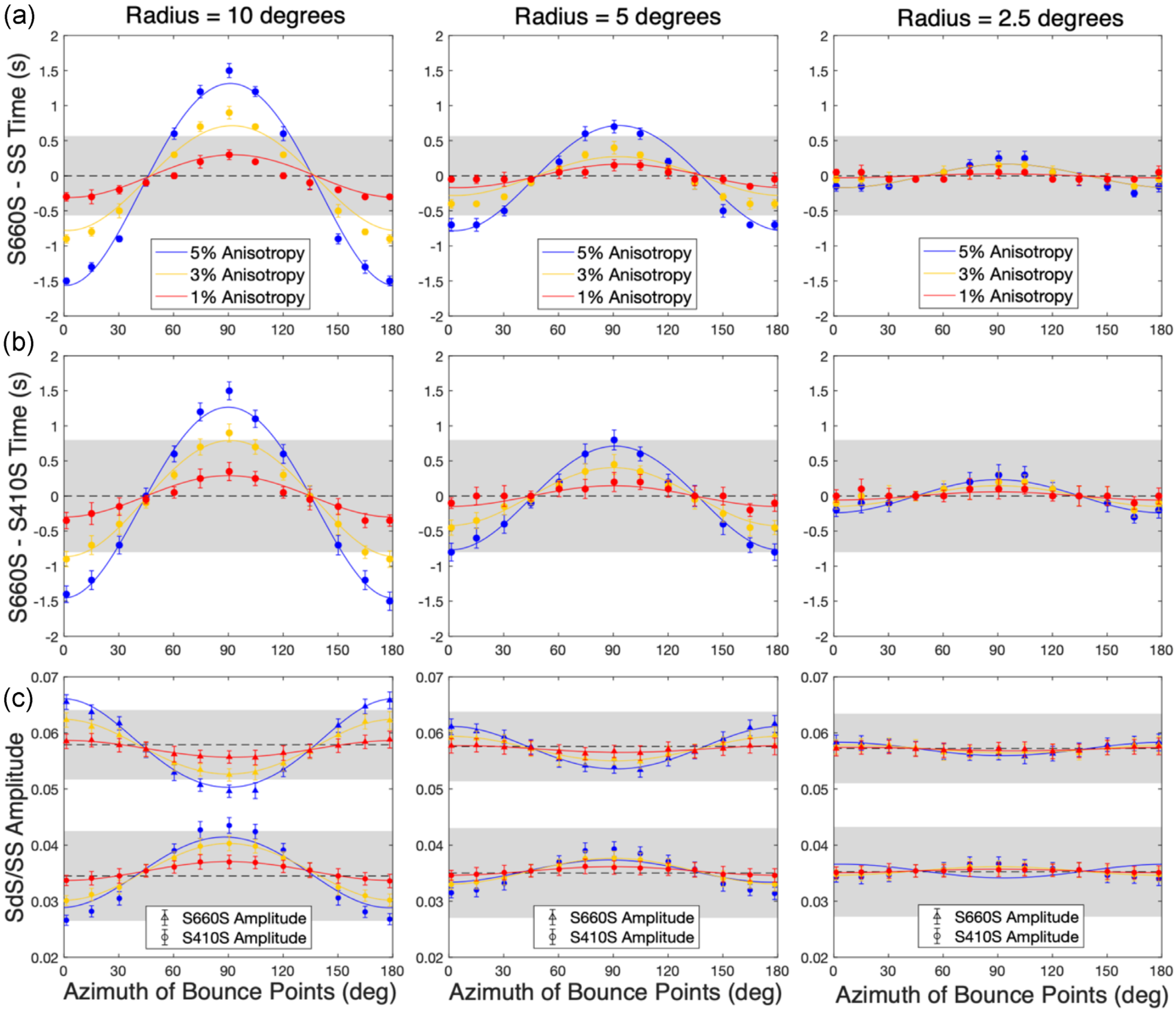

Figure 7. Effects of anisotropy size and strength on SS precursors. The measurements of (a) S660S−SS time residuals, (b) S660S−S410S time residuals, (c) S410S/SS and S660S/SS amplitudes are shown as a function of bounce point azimuths. The radius of anisotropy decreases from 10° to 5° and 2.5° from left to right, whereas the bin radius remains 10°. The depth of anisotropy is in the MTZ (400–670 km). The solid curves represent the best-fitting models for 1, 3 and 5 per cent input anisotropy. The dashed lines denote the mean values of each measurement. The grey shaded regions represent the detection thresholds for SdS traveltimes and amplitudes estimated from the stacking of synthetics with an average noise level (SNR = 7).

significantly above zero either. The inversions suggest that the MTZ anisotropy is very weak in the central Pacific, and we cannot distinguish the signal from a null result.

To further test the weak anisotropy hypothesis, we added noise to the 3-D synthetics (see Section 2.2) with different SNR values, using both idealized and realistic geometries to explore the effect of data coverage in the central Pacific region (Fig. 2). The goal was to test the resolution of the SS precursors in the central Pacific region, and determine the minimum strength of anisotropy that would provide a detectable signal in the data. To quantify detectability of anisotropy, we define a parameter ε as the total misfit of the best-fitting model compared to the input anisotropy model:

$$\varepsilon_G = \sqrt{\left(\frac{\mathrm{dln}G_{\mathrm{out}} - \mathrm{dln}G_{\mathrm{in}}}{\mathrm{dln}G_{\mathrm{in}}}\right)^2 + \left(\frac{2\sigma_G}{\mathrm{dln}G_{\mathrm{out}}}\right)^2}, \tag{6}$$

$$\varepsilon_\Theta = \sqrt{\left(\frac{\Theta_{\mathrm{out}} - \Theta_{\mathrm{in}}}{\pi/2}\right)^2 + \left(\frac{2\sigma_\Theta}{\pi/2}\right)^2}, \tag{7}$$

where ε_G and ε_Θ are the total misfit for strength of anisotropy and fast direction, respectively, $\mathrm{dln}G_{\mathrm{in}}$ and Θ_{in} are the input strength of anisotropy and input fast direction, respectively, $\mathrm{dln}G_{\mathrm{out}}$ and σ_G are the best-fitting strength of anisotropy and 1σ error from inversions, respectively, Θ_{out} and σ_Θ are the best-fitting fast direction and 1σ error, respectively. ε can quantify the detectability of anisotropy as it takes into account the misfit between the input and best-fitting anisotropy parameters, and the uncertainties of the best-fitting model as well. ε is a positive value, and if $\varepsilon < 1$, we define this scenario as a detectable case. Conversely, if $\varepsilon \geq 1$, we define this scenario as a non-detectable case. Since ε represents the misfit of the best-fitting model, the larger this value is, the lower the detectability.

For the idealized geometry models, the detectability of anisotropic variations from SdS traveltimes and amplitudes are shown in Fig. 10. Generally, the detectability of anisotropy increases as the input anisotropy increases or the noise level decreases. Fig. 10(a) illustrates that the S660S−S410S time can detect 3 per cent anisotropy with an intermediate level of noise (SNR = 7). Fig. 10b suggests that the S660S−SS time has better resolution and can detect 3 per cent anisotropy even with higher levels of noise (SNR = 4). However, our tests with shallow anisotropy demonstrate that S660S−SS time is also potentially affected by the upper mantle

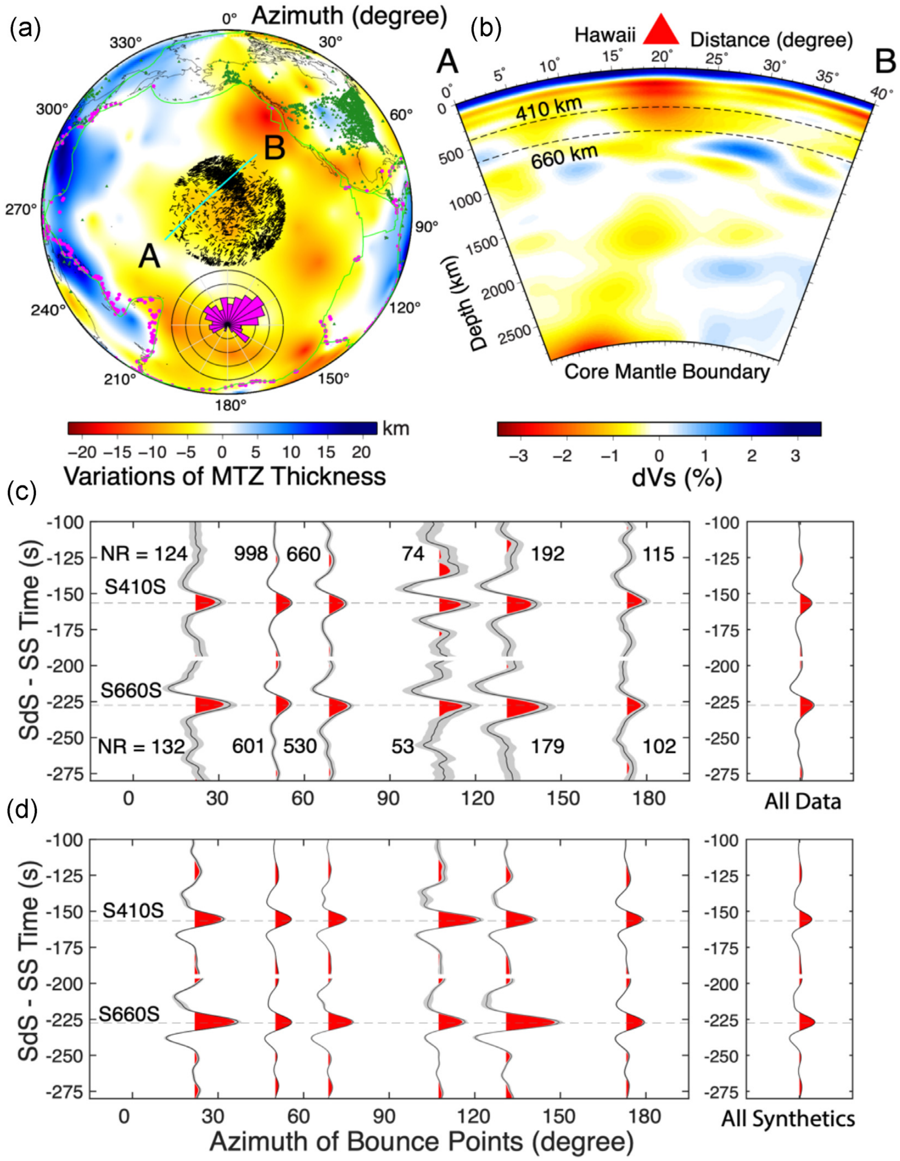

Figure 8. (a) Central Pacific bin of SS precursor data superimposed on the MTZ topography map. The MTZ thickness from Huang *et al*. (2019) is expressed as the variations with respect to the global mean value 244.4 km. The black bars represent the SS bounce points and the azimuths of SS ray paths. The radius of the bin is 2000 km. The pink circles denote the earthquakes and the green triangles represent the stations. The green curves are the plate boundaries (DeMets *et al*. 1990). The rose diagram shows the azimuthal coverage of SS bounce points in log scale. The cyan line highlights the location of cross-section AB. (b) A cross-section of S40RTS tomography model (Ritsema *et al*. 2011) illustrating the slow V_S anomalies beneath Hawaiian hotspot that has been interpreted as a mantle plume rising from the core mantle boundary. The red triangle denotes the location of Hawaii. The azimuthal stacking results of the (c) data and (d) synthetics in the central Pacific bin. The number of records (NR) of each azimuthal bin is labelled beside the waveform. The dashed lines highlight the average SdS traveltimes from the stacking of all data or synthetics in this region, which are shown in the right-hand panels.

structure (Fig. 4c), so it is not an independent indicator for MTZ anisotropy. The test also indicates that S410S and S660S amplitudes have lowered resolutions compared to the traveltime metrics. The S410S amplitude can only resolve 5 per cent anisotropy with intermediate level of noise (Fig. 10c), and the detectability of anisotropy with the S660S amplitude is always low even when noise is absent (Fig. 10d). When using a more realistic geometry model, detectability is further degraded due to the lack of stations in the southern Pacific (Fig. S3). However, despite the incomplete azimuthal coverage, our tests prove that the S660S−S410S time should present a detectable traveltime anomaly where there is 3 per cent anisotropy in the central Pacific region (Fig. S3a). The conclusion is that the central Pacific data have the potential to resolve 3 per cent or greater anisotropy but did not detect an anomaly of this magnitude. As a result, the azimuthal anisotropy in this region is likely to be smaller than 3 per cent.

3.3 Japan subduction zone

In our previous study (Huang *et al*. 2019), we found evidence for ∼3 per cent MTZ anisotropy beneath the circum-Pacific subduction zones. However, the results were based on the stacking of multiple subduction zones, so there was ambiguity about where the signal originated, or if it was ubiquitous amongst all subduction zones. Due to the relatively high density of data, we identified the Honshu

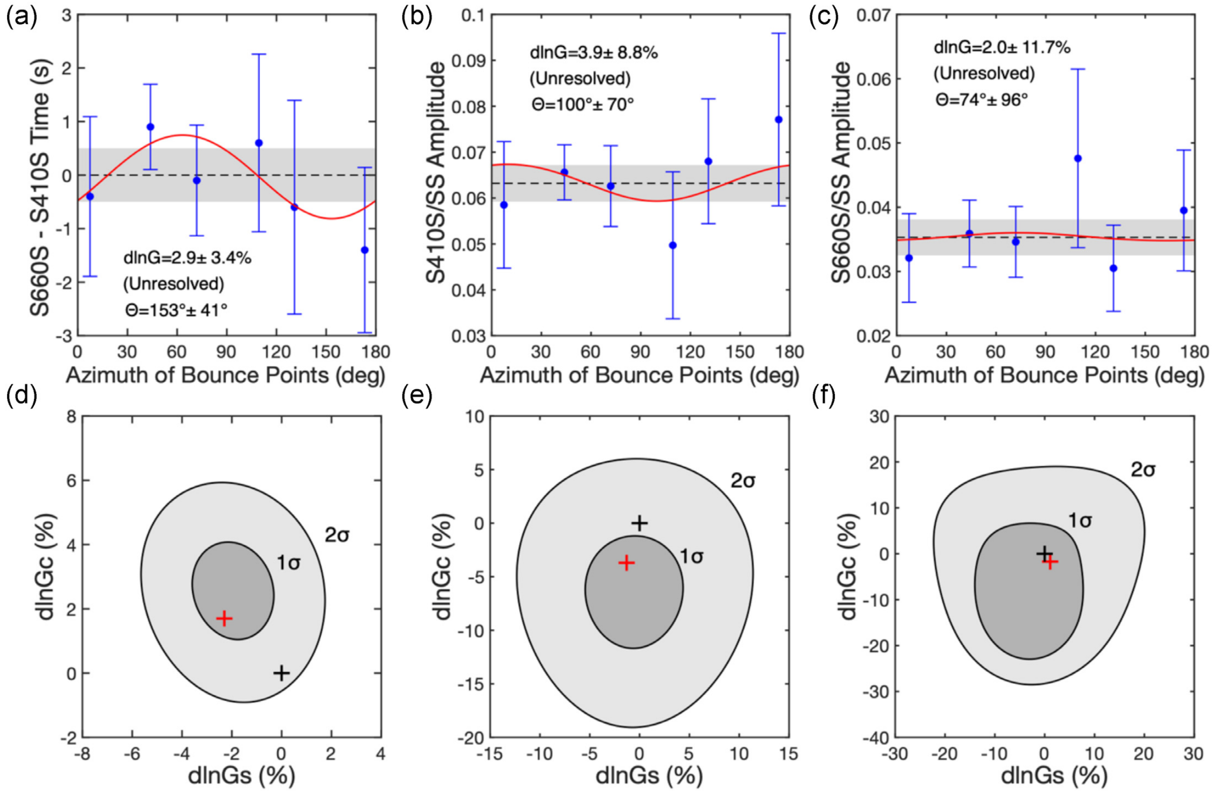

Figure 9. Measurements of (a) S660S−S410S time residuals, (b) S410S/SS amplitude and (c) S660S/SS amplitude are shown as a function of bounce point azimuths from the stacking results in the central Pacific region. The error bars denote the 2 σ uncertainties of each measurement. The dashed lines represent the mean values for each measurement from the stacking of all azimuthal bins, and grey shaded boxes are the corresponding 2σ errors. The red curves represent the best-fitting anisotropy models from grid-search. The dlnG and Θ values in each panel are the best-fitting strength of anisotropy and fast direction, respectively. The grid-search results for S660S−S410S time residuals, S410S/SS amplitude and S660S/SS amplitude are shown in panel (d), (e) and (f), respectively. The red cross denotes the best-fitting model and black cross represents the zero-anisotropy model. The error ellipses represent the 1 σ and 2σ uncertainties of the best-fitting model based on chi-squared statistics.

subduction zone near Japan as a study region to uniquely determine the character of MTZ anisotropy. The Honshu subduction zone is located in a region where the MTZ is thickened primarily due to the cold slab (e.g. Tian *et al*. 2016; Fig. 11a). The EARA2014 tomography model (Chen *et al*. 2015) shows that the subducting slab appears to be lying horizontally above the 660-km discontinuity beneath Northeast (NE) China (Fig. 11b). Other regional tomography models also show a similar flat feature of the slab (e.g. Huang & Zhao 2006; Fukao & Obayashi 2013; Wei *et al*. 2015; Tao *et al*. 2018).

We chose this region to study the mantle deformation associated with the flat slab, since it is the best-sampled subduction zone in our SS data set. Similar to the central Pacific region, we also divided the data into 30° azimuthal bins. However, the azimuthal coverage is relatively poor, with only four usable azimuthal bins for stacking and especially lacking the data with east-west orientations (Fig. 11a). The azimuthal stacking results of data and synthetics are illustrated in Figs 11(c) and (d), respectively. Despite limited data coverage, the S410S and S660S are still recovered from stacking in all these four bins, noting that the S410S in the 90° bin (NR = 3) is relatively noisier.

We first inverted the strength of anisotropy and fast direction from the S660S−S410S time residuals (Fig. 12a). The S660S−S410S time residuals for each azimuthal bin are calculated as the travel-time differences between the stacking results of all data in the Japan subduction zone and the respective bins. The inversion suggests that strong MTZ anisotropy (dlnG = 15.3 ± 2.7 per cent) exists in this region with a trench-perpendicular fast direction (Θ = 93° ± 5°). Unlike the central Pacific region, the chi-squared statistical test indicates that the MTZ anisotropy is significantly above zero (Fig. 12d). To test if our result is biased by the EARA2014 model, we also used another high-resolution tomography model FWEA18 (Tao *et al*. 2018) as well as a global model S40RTS (Ritsema *et al*. 2011) for additional tomography corrections. The comparisons between these two regional models and S40RTS model are illustrated in Figs S4 and S5. We find that the strength of anisotropy is dependent on the tomography corrections. From the inversions, we obtain a slightly weaker anisotropy (dlnG = 11.4 ± 7.9 per cent, Fig. S6a) using the S40RTS model, but a stronger signal (dlnG = 17.5 ± 4.4 per cent, Fig. S6c) using the FWEA18 model. These discrepancies arise from the different amplitudes of V_S anomalies in these tomography models: a global tomography model like S40RTS is generally smoother than regional tomography models, and likely underestimates the V_S anomalies near the slab (Figs S4–S5). Therefore, we recomputed the uncertainty of dlnG by accounting for the V_S uncertainties from the tomography models, and the new estimate is dlnG = 15.3 ± 9.2 per cent. The inversion results for fast directions are very similar among these three models: Θ = 92° ± 23° for S40RTS model (Fig. S6a) and Θ = 92° ± 8° for FWEA model (Fig. S6c). The chi-squared statistical tests show that all three anisotropy inversions are significantly above zero (Figs S6d–f), which further supports that the observed MTZ anisotropy is a robust signal.

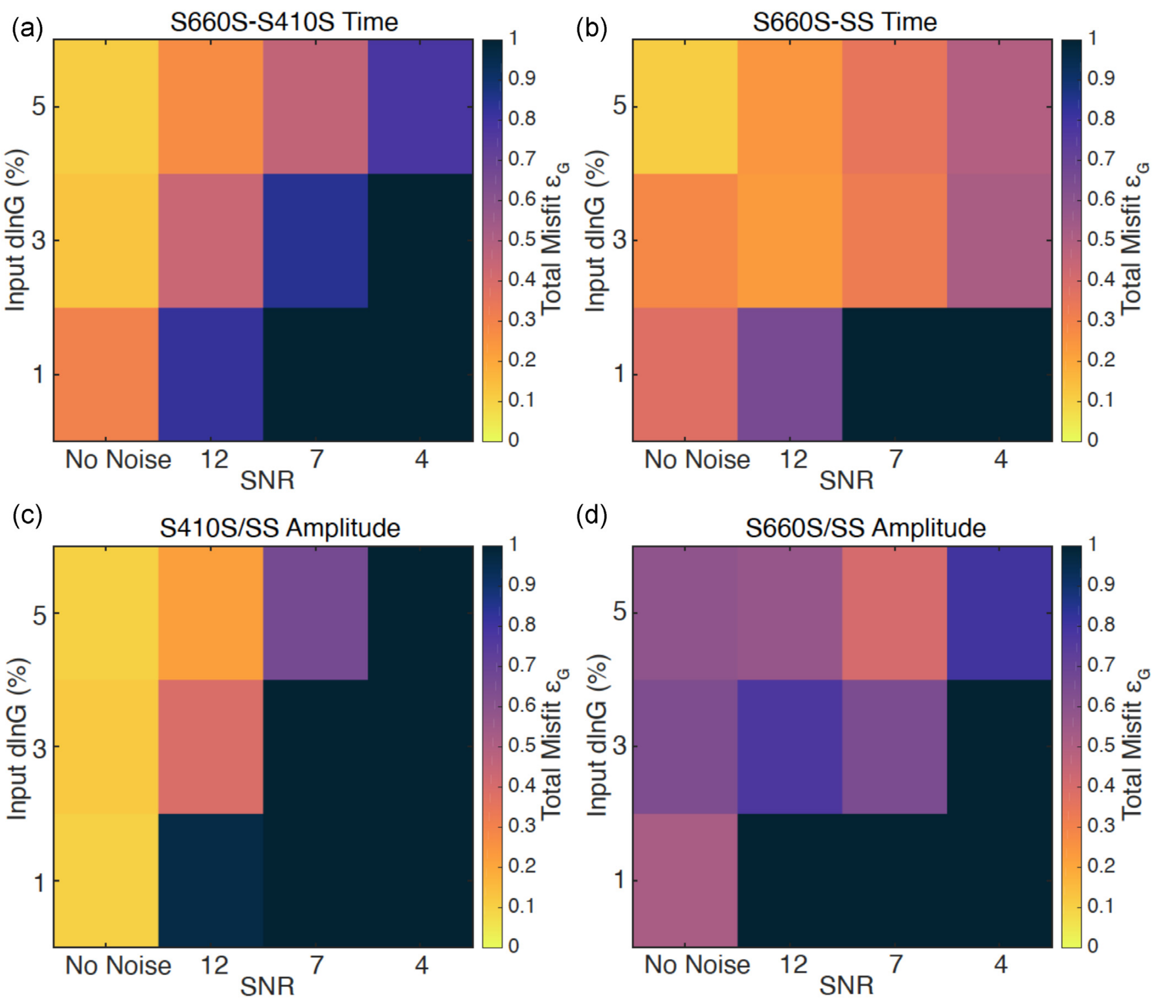

Figure 10. Detectability matrix for the central Pacific bin using an idealized source–receiver geometry. The dlnG detectability matrix for (a) S660S−S410S time, (b) S660S−SS time, (c) S410S/SS amplitude and (d) S660S/SS amplitude. SNR = 7 is the average noise level of our SS data set. The total misfit ε_G of dlnG is negatively correlated with the detectability. When ε_G is greater than 1 (saturated in the plot), the model is considered as non-detectable.

The inversions for S410S/SS and S660S/SS amplitudes are shown in Figs 12(b) and (c), respectively. The strength of anisotropy (dlnG = 19.2 ± 18.0 per cent) inverted from S410S/SS amplitudes is significantly above zero (Fig. 12e), and this value is consistent with the one inverted from S660S−S410S time. On the contrary, the inversions for S660S/SS amplitudes show larger uncertainties, thus not significantly above zero (Fig. 12f). This suggests that the MTZ anisotropy likely exists in the upper transition zone right below the 410-km discontinuity, thereby causing the change of reflection coefficients of S410S with azimuths. Similar to the S660S−S410S time, we also tested other two tomography models to validate this anisotropy signal. However, the inversions for S410S/SS amplitudes based on other two tomography models are not significantly above zero (Figs S7d and f). We therefore conclude that the MTZ anisotropy constrained from S410S/SS amplitudes is not a robust signal, and this should not be used for further interpretations.

Following the Central Pacific study region methodology, we ran a similar resolution test for the Japan subduction zone using both idealized and realistic source and receiver geometries (Fig. 3) but with stronger anisotropy. The resolution of the idealized geometry model is very similar to that of the central Pacific region although the bin size is smaller. However, the realistic geometry model using the actual azimuthal coverage of Japan bin displays poorer detectability in Fig. 13. Despite the lower resolution, Fig. 13(a) demonstrates that S660S−S410S time can detect ∼15 per cent anisotropy with intermediate level of noise (SNR = 7). Fig. 13(b) reveals that the detectability of fast direction is even higher: S660S−S410S time can reconstruct the input fast direction as long as anisotropy is greater than 5 per cent. This resolution test and chi-squared statistical test both suggest that the MTZ anisotropy observed in the Japan subduction zone is a robust feature. On the contrary, the detectabilities of S410S/SS (Fig. 13c) and S660S/SS amplitudes (Fig. 13d) are much lower, which is consistent with the non-detection of MTZ anisotropy from the amplitude inversions in Fig. 12.

4 DISCUSSION

4.1 Proof of concept: resolutions and limitations of SS precursors

Currently, the two major tools to constrain deep mantle anisotropy are shear wave splitting and higher mode surface waves. However, the shear wave splitting method has limited vertical resolution to distinguish the depth distribution of anisotropy, while surface waves

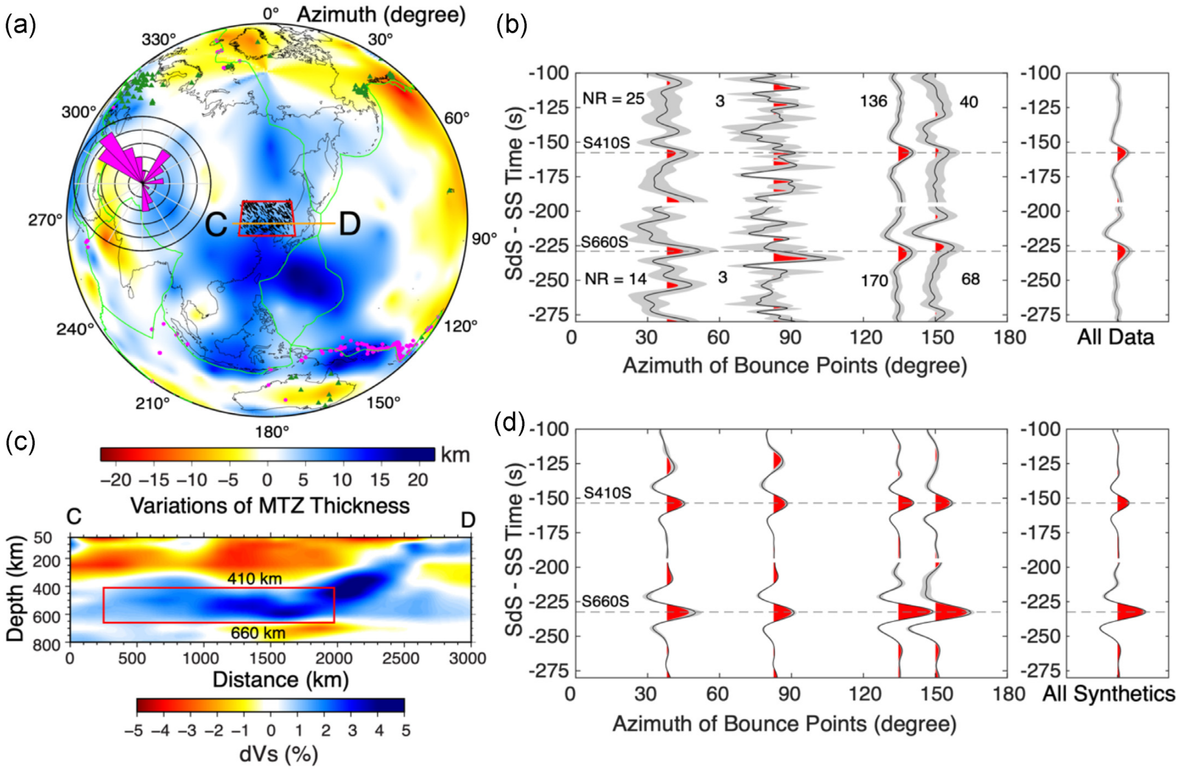

Figure 11. (a) SS precursor data in the Japan subduction zone superimposed on the MTZ topography map. The legends are the same as Fig. 8. The study region is highlighted by the red box, and the size is 1500 km × 1000 km. The rose diagram shows the azimuthal coverage in log scale. The orange line shows the location of cross-section CD. (b) A cross-section of EARA2014 tomography model (Chen *et al*. 2015) showing the flat slab in the MTZ. The red box highlights our study region. The azimuthal stacking results of the (c) data and (d) synthetics in the Japan subduction zone. The number of records (NR) of each azimuthal bin is labelled beside the waveforms. The dashed lines highlight the average SdS traveltimes from the stacking of all data or synthetics in this region, which are shown in the right panels.

have low horizontal resolution (∼6500 km in the MTZ from Visser *et al*. 2008; Yuan & Beghein 2018) and cannot detect small-scale anisotropy such as the structures near subduction zones. For comparison, the horizontal resolutions of long-period SS precursors (i.e. Fresnel zone) are ∼1000 km in radius (e.g. Dahlen 2005; Lawrence & Shearer 2008). We have demonstrated that stacks of the SS precursors have sensitivity to azimuthal anisotropy in the upper mantle and MTZ through 3-D synthetic modelling. The traveltimes of SS precursors can detect ≥3 per cent azimuthal anisotropy in the MTZ with intermediate level of noise (SNR = 7). The amplitudes of SS precursors can shed light on the anisotropy change across a seismic discontinuity such as the 410-km discontinuity (Saki *et al*. 2018). Due to the effect of stacking, the uncertainties of SdS amplitudes are often larger than traveltime measurements so they can only detect ≥5 per cent azimuthal anisotropy in the MTZ. However, we can apply this method to a shallower upper mantle discontinuity with stronger anisotropy such as the lithosphere-asthenosphere boundary (LAB) or mid-lithosphere discontinuity (MLD) where the polarity change of the amplitudes can take place (e.g. Rychert *et al*. 2014; Wirth & Long 2014).

Sufficient azimuthal coverage is key to successfully applying SS precursors to anisotropy studies. This method requires at least 4–5 different azimuths with NR > 100 in each azimuthal bin to obtain a robust estimate of strength and fast direction of anisotropy. However, insufficient azimuthal coverage is common in our SS data set, and we only identify four candidate locations suitable for constraining azimuthal anisotropy: (1) the northwestern Pacific, (2) the central Pacific, (3) the central Atlantic and (4) Greenland (Huang *et al*. 2019). This is primarily due to the uneven distributions of large earthquakes concentrated near plate boundaries and dense stations mostly in North America (e.g. USArray). This means that although the western Pacific subduction zones have large numbers of records sampling the region, azimuthal coverage is actually quite limited. However, in the Japan subduction zone, we have demonstrated that a strong anisotropy (>10 per cent) can still be detected by SS precursors when azimuthal coverage is limited. The data could be augmented by future ocean bottom seismometers (OBS) deployed across the Pacific Ocean (e.g. Kawakatsu *et al*. 2009).

A second challenge identified in this approach is the determination of the depth and thickness of the anisotropic layer. Our tests show that the SS precursors cannot resolve multiple sublayers of anisotropy structures in the target depth range (Fig. S2). For example, the SS precursors cannot distinguish whether MTZ anisotropy is located in the upper or lower MTZ, or the whole MTZ. Thus, in our modelling and data analysis, we only assume uniform anisotropy across the whole MTZ, which may underestimate the strength of anisotropy if it is only localized in a sublayer. The final challenge is that we focus only on the SH waves to constrain azimuthal anisotropy, but SV waves can also provide useful information about anisotropy, via the splitting of the SS phase and its precursors (e.g. Wolfe & Silver 1998). Furthermore, there might be potential contaminations from the leakage of SV waves (e.g. SKKKS phase) to the transverse component due to the inaccurate

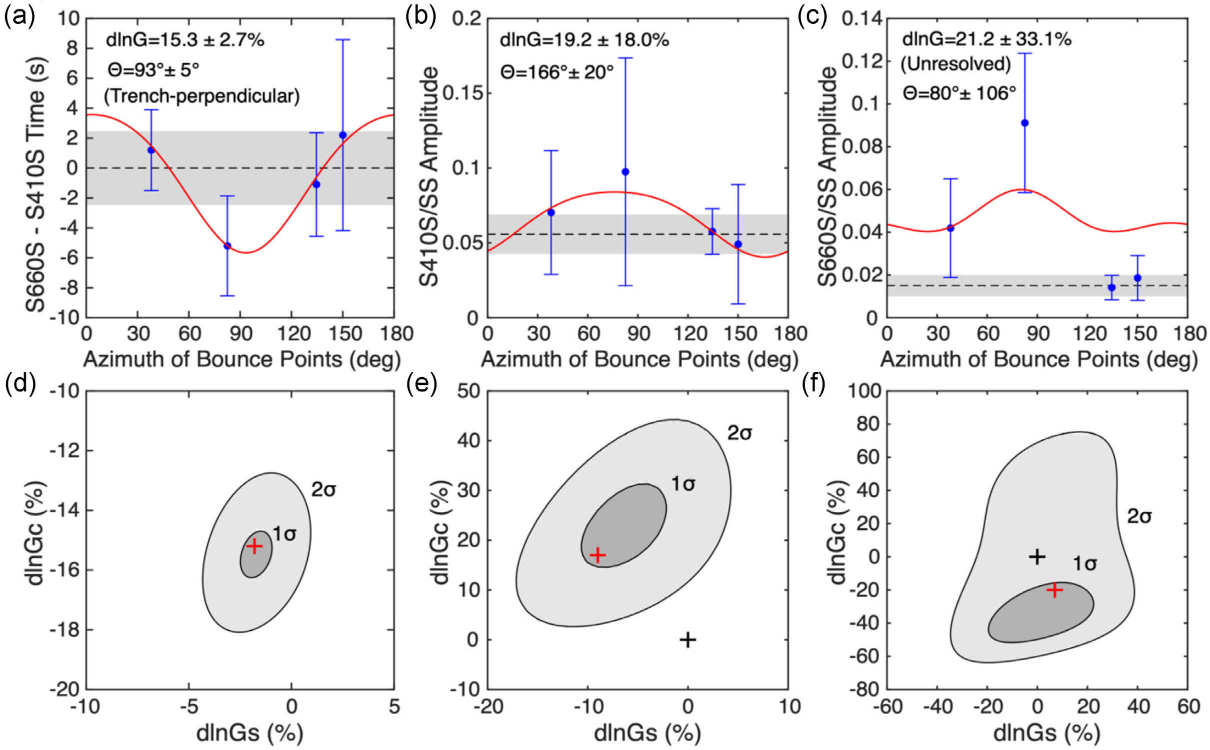

Figure 12. Measurements of (a) S660S−S410S time residuals, (b) S410S/SS amplitude and (c) S660S/SS amplitude are shown as a function of bounce point azimuths from the stacking results in the Japan subduction zone. The legends are the same as Fig. 9. The red curves denote the best-fitting anisotropy models. The grid-search results for S660S−S410S time, S410S/SS amplitude and S660S/SS amplitude are shown in panels (d), (e) and (f), respectively. The red cross denotes the best-fitting model and black cross represents the zero-anisotropy model. The error ellipses represent the 1 σ and 2σ uncertainties of the best-fitting model derived from chi-squared statistics. The azimuthal anisotropy inverted from S660−S410S time is significantly above zero and shows a trench-perpendicular fast direction.

rotations of horizontal components. However, even if the inaccurate rotations exist, the amplitudes of these phases are still much smaller than that of SS precursors on the transverse component, thus would only cause negligible interference (Waszek *et al*. 2018). Despite these limitations, SS precursors can serve as a new method to constrain seismic anisotropy in the upper and mid-mantle, especially beneath oceanic regions where seismic stations are underpopulated for shear wave splitting measurements.

4.2 Mantle deformation in the transition zone

4.2.1 Hawaiian hotspot

In the central Pacific region, we did not find definitive evidence for MTZ anisotropy beneath the Hawaiian hotspot. Few shear-wave splitting studies have reported evidence for MTZ anisotropy in this region, either due to the interference of strong lithosphere and asthenosphere anisotropy (e.g. Collins *et al*. 2012) or simply lack of data. Therefore, we compare our results to three higher mode surface wave models at 500-km depth: YB13SVani (Yuan & Beghein 2013), SL2016SvA (Schaeffer *et al*. 2016), and 3D2017_09Sv (Debayle *et al*. 2016). These three models only show 0.5–1.0 per cent azimuthal anisotropy near Hawaiian hot spot. Ideally, the SS precursors can only detect 1 per cent azimuthal anisotropy with very clean data (SNR > 12, Fig. 10). In this case, the strength of MTZ anisotropy beneath Hawaiian hot spot is likely below our resolution. This suggests that the vertical mantle flow associated with the Hawaiian plume has not produced significant MTZ azimuthal anisotropy (Fig. 14).

4.2.2 Deformation in the flat slab

In the Japan subduction zone, we found evidence for strong azimuthal anisotropy (15.3 ± 9.2 per cent) in the MTZ with a trench-perpendicular fast direction. We note that the uncertainty of MTZ anisotropy is as large as 9.2 per cent due to the limited data coverage in Japan as well as the additional uncertainties arising from the tomography models used for the traveltime corrections. The lower bound of MTZ anisotropy (∼6 per cent) approaches the mineral physics constraints on the maximum anisotropy expected from the MTZ minerals. Although wadsleyite is considered as the main contributor to MTZ anisotropy, a > 6 per cent anisotropy signal cannot be readily explained solely by LPO of wadsleyite. Furthermore, the addition of water near the slab would decrease the elastic anisotropy of wadsleyite (Zhang *et al*. 2018; Zhou *et al*. 2021), making it more difficult to explain such a strong anisotropic signal. Similarly, LPO of metastable olivine wedge within the slab is not predicted to produce a >6 per cent anisotropy signature either (e.g. Kawakatsu & Yoshioka 2011). Another seismological study by Li *et al*. (2018) observed even stronger V_S anisotropy (15–25 per cent) in the MTZ near Japan, which was attributed to the presence of highly anisotropic mineral magnesite (∼40 per cent V_S anisotropy, Yang *et al*. 2014) layered into the slab. As discussed in Section 4.1, long-period SS precursors would likely underestimate the strength of anisotropy

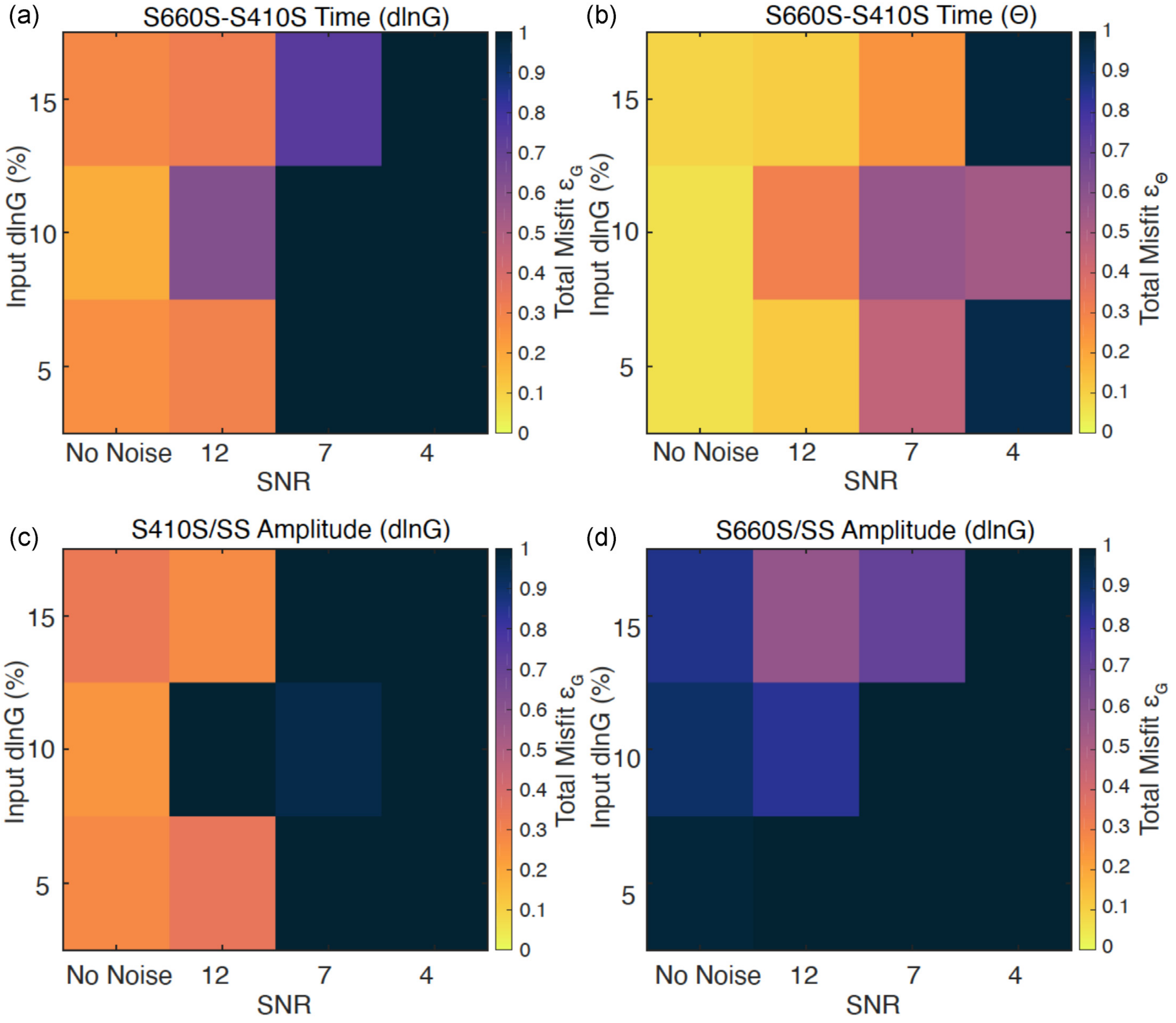

Figure 13. Detectability matrix for the Japan subduction zone using a realistic source–receiver geometry. The (a) dlnG and (b) Θ detectability matrix for S660S−S410S time. The dlnG detectability matrix for (c) S410S/SS amplitude and (d) S660S/SS amplitude.

from the 10 to 100 km small-scale structures as observed by Li *et al*. (2018). Given the complex chemical heterogeneities present in subduction zones, it is likely that more than one mineralogical mechanism contributed to these complex systems.

For example, the presence of other highly anisotropic minerals, such as stishovite in the upper basalt layer or akimotoite in the lower harzburgite layer, would be expected in the flat slab beneath NE China, and thus might contribute to the observed MTZ anisotropy. Stishovite would form in the mid-ocean ridge basalt at 10–20 vol per cent, and it has a single crystal V_S anisotropy that can reach up to ∼49 per cent (e.g. Cordier *et al*. 2004; Jiang *et al*. 2009; Xu *et al*. 2020). Geodynamic modelling demonstrates that the MTZ could be a basalt-enriched reservoir with a basalt fraction between 30 and 50 per cent (Yan *et al*. 2020). However, even given the potential basalt enrichment, the volume fraction of stishovite could only reach up to ∼10 per cent across the MTZ, so the resulting anisotropy caused by the LPO of stishovite would be less than 1 per cent (Faccenda *et al*. 2019). Another possibility is that akimotoite could be stable in the lower MTZ, especially in cold subduction zones, and it has been proposed to be a contributor to MTZ anisotropy observed in the Tonga subduction zone due to its large V_S anisotropy between 18 and 25 per cent (e.g. Shiraishi *et al*. 2008; Hao *et al*. 2019). However, the volume fraction of akimotoite is estimated to be only ∼15 per cent in harzburgite (Ishii *et al*. 2019), thereby again yielding less than 1 per cent anisotropy in the MTZ. Since the subducting slab can potentially transport water into the MTZ, hydrous phases (e.g. Nowacki *et al*. 2015) and extremely anisotropic mineral ice-VII (70 per cent V_S anisotropy, Zhang *et al*. 2019) are candidates for contributing to the observed anisotropy as well. However, the scales of these structures are likely small, thereby not producing detectable anisotropy by SS precursors. Owing to their low expected abundances, the LPO of highly anisotropic minerals within the slab alone do not seem to explain the strong MTZ anisotropy either.

An alternative mechanism is that the SPO associated with the compositional layering in the slab could explain the observed MTZ anisotropy. Theoretical calculations show that the extrinsic V_S anisotropy caused by the grain-scale SPO in the basaltic materials could reach up to 6 per cent (Faccenda *et al*. 2019). This is compatible with the lower bound of observed MTZ anisotropy beneath NE China. Furthermore, global thermochemical convection models show that the lower MTZ is potentially enriched in basalt (Ballmer *et al*. 2015; Yan *et al*. 2020), thus providing sufficient source of extrinsic anisotropy. Therefore, the grain-scale SPO of basaltic materials induced by the shear deformation within the flat

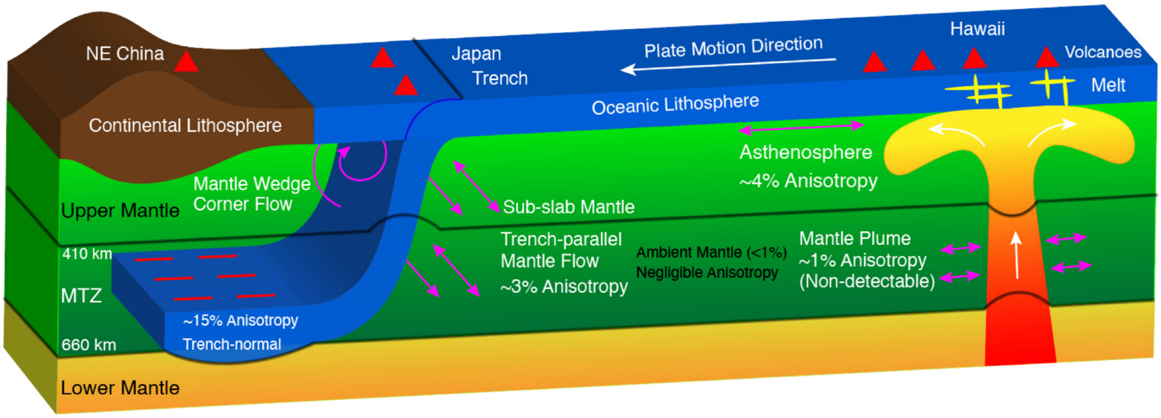

Figure 14. A schematic diagram depicting the deformation in the upper mantle and transition zone observed from SS precursors. The red lines on the left represent the grain-scale SPO of basaltic materials (Faccenda *et al.* 2019) that produced the strong azimuthal anisotropy (15.3 ± 9.2 per cent) in the flat slab beneath NE China. The pink arrows denote the inferred mantle flow direction from azimuthal anisotropy assuming A-type olivine in the upper mantle and [001] (010) slip system of wadsleyite in the MTZ (Kawazoe *et al.* 2013). On the left, the trench-parallel flow consistently exists in the subslab upper mantle and MTZ beneath the Japan subduction zone (Huang *et al.* 2019). The mantle wedge is likely dominated by the trench-perpendicular corner flow (e.g. Zhao *et al.* 2009) which is not observed in our study. On the right, the Hawaiian mantle plume can only produce very weak azimuthal anisotropy (∼1 per cent) which is not detectable from SS precursors. The asthenosphere beneath Hawaii show strong azimuthal anisotropy (∼4 per cent) with a fast direction parallel to the plate motion direction (Huang *et al.* 2019). The azimuthal anisotropy is negligible (<1 per cent) in the ambient mantle. The red triangles represent the volcanoes associated with hotspots or subduction zones.

slab is a plausible mechanism to explain the strong MTZ anisotropy beneath NE China (Fig. 14). However, we cannot rule out that the LPO of anisotropic minerals (e.g. wadsleyite, stishovite and akimotoite) also contributes to the observed MTZ anisotropy, even though their influence could be small. Since the grain-scale SPO is only compatible with the lower bound of MTZ anisotropy, it is very likely that a combination of LPO and SPO or other mechanisms together all contributed to the observed MTZ anisotropy. Joint modelling of LPO and SPO mechanisms within the MTZ is required to determine whether larger degrees of anisotropy can be achieved with complex compositional heterogeneities.

The trench-perpendicular fast direction is consistent with previous observations using source-side shear wave splitting measurements of deep earthquakes beneath NE China (e.g. Lynner & Long 2015; Nowacki *et al.* 2015). Lynner & Long (2015) found evidence for azimuthal anisotropy originating from the MTZ and uppermost lower mantle beneath NE China, and the fast splitting direction is also trench-perpendicular. The *P*-wave anisotropic tomography study also detected trench-perpendicular fast direction located in the flat slab (Wei *et al.* 2015). The consistency among these three different methods combined with our 3-D synthetic modelling suggests that trench-perpendicular anisotropy is a definitive feature of the MTZ beneath NE China. However, the fast splitting directions in the MTZ display a heterogeneous pattern across different subduction zones around the Pacific Ocean. Beneath the Tonga subduction zone, the dominant fast direction is trench-parallel (Foley & Long 2011; Mohiuddin *et al.* 2015); whereas the Sumatra and South America subduction zones show both trench-parallel and trench-perpendicular fast directions (di Leo *et al.* 2012; Lynner & Long 2015; Nowacki *et al.* 2015). Our previous study (Huang *et al.* 2019) combined all the data in the circum-Pacific subduction zones for stacking and concluded that trench-perpendicular fast direction is the most coherent pattern, however our data could have been biased by the regions in Japan and South America where the data coverage is the densest. The variability of fast directions also suggests heterogeneous flow patterns associated with different subducting slabs (penetrating or stagnant) in the mid-mantle, and may be indicative of which underlying physical mechanisms are responsible for the observed anisotropy.

4.2.3 Trench-parallel flow in the subslab mantle

To provide a holistic view of mantle flow and deformation pattern near or within the subducting slabs, we combined this study with our previous observations of MTZ anisotropy using SS precursors (Huang *et al.* 2019) for further discussions. In this study, we used a regional data set which is mainly sensitive to the slab deformation beneath NE China. However, in Huang *et al.* (2019), our data were more sensitive to the subslab mantle anisotropy rather than the subducting slab itself, thus shedding more light on the mantle flow patterns beneath the slab. The strength of subslab MTZ anisotropy is only ∼3 per cent which is much weaker than the observed anisotropy in the flat slab. Therefore, unlike the interpretations above, we can assume that LPO of wadsleyite is the primary contributor to the MTZ anisotropy in the subslab mantle beneath Japan. The interpretation of mantle flow direction from the fast direction of mantle anisotropy requires the experimental data of wadsleyite's dominant slip systems (Sharp *et al.* 1994; Thurel & Cordier 2003; Demouchy *et al.* 2011; Kawazoe *et al.* 2013; Ohuchi *et al.* 2014). Kawazoe *et al.* (2013) reported that the dominant slip system of wadsleyite is [001] (010), therefore the mantle flow direction is perpendicular to the fast polarization direction of shear wave, which is the same as B-type olivine (e.g. Jung & Karato 2001). Under the assumption of a [001] (010) slip system for wadsleyite, the seismic trench-perpendicular fast direction then infers trench-parallel flow in the subslab MTZ (Fig. 14). The inferred flow also agrees well with the trench-parallel flow directions in the subslab MTZ predicted by 3-D geodynamic modelling (Faccenda 2014).

Our previous study (Huang *et al.* 2019) also reported that trench-parallel fast direction is dominant in the upper mantle (<410 km) beneath the slab, which is consistent with trench-parallel flow assuming A-type olivine fabric (e.g. Karato *et al.* 2008). The trench-parallel flow around slabs agrees well with the toroidal flow induced by trench migration (Faccenda & Capitanio 2012). Consequently, our results suggest that the mantle flow direction remains consistently trench-parallel throughout the entire subslab upper mantle and transition zone beneath Japan (Fig. 14). Alternatively, the flow direction in the transition zone can rotate by 90° and become trench-perpendicular if we assume a different type of slip system of wadsleyite (e.g. Demouchy *et al*. 2011), but this is less consistent with geodynamic modelling (Faccenda 2014).

5 CONCLUSION

We have investigated the sensitivity of SS precursors to azimuthal anisotropy using 3-D synthetics computed from SPECFEM3D_GLOBE. We tested the following factors that affect the sensitivity of SS precursors: the depth of anisotropy, size and strength of anisotropy, source and receiver geometry, and noise level. We demonstrate that the SS precursors can distinguish between anisotropy in the upper mantle versus the MTZ via the azimuthal variations of SdS traveltimes and amplitudes. The source and receiver geometry (i.e. azimuthal coverage) plays a key role in constraining the strength of anisotropy and fast direction. When data coverage is sufficient (i.e. $\mathrm{NR} > 100$ in each azimuthal bin), the SS precursors can resolve ≥ 3 per cent azimuthal anisotropy in the MTZ where stacked data have an average level of noise ($\mathrm{SNR} = 7$). In case of biased or limited azimuthal coverage (e.g. Japan), the strength of anisotropy and fast direction were still recovered from our analysis of S660S−S410S time when the local anisotropy is strong (>10 per cent).

We used our approach to search for evidence for mantle flow associated with a mantle plume or subducting slab in the MTZ beneath the central Pacific region and the Japan subduction zone. In the Japan subduction zone, we detected significant azimuthal anisotropy ($\mathrm{dlnG} = 15.3 \pm 9.2$ per cent) with a trench-perpendicular fast direction ($\Theta = 93^\circ \pm 5^\circ$) in the MTZ. We attribute this V_S anisotropy to the grain-scale SPO of basaltic materials induced by the shear deformation in the flat slab beneath NE China. It is likely that the LPO of wadsleyite and other highly anisotropic minerals (e.g. stishovite and akimotoite) introduced by the subducting slab also contributed to this anisotropic signal. The relatively weaker anisotropy (∼3 per cent) observed in the subslab MTZ is attributed to the LPO of wadsleyite such that the trench-perpendicular fast direction in Japan is interpreted as trench-parallel mantle flow based on the dominant slip system of wadsleyite. We infer that the mantle flow direction beneath Japan is likely to remain consistently trench-parallel throughout the entire subslab upper mantle and transition zone. In the central Pacific region, the resolution test suggests that our data can resolve 3 per cent anisotropy, but no anisotropy is detected. The MTZ anisotropy is probably $<<3$ per cent beneath central Pacific, which is consistent with ∼1 per cent anisotropy from the surface wave models, and therefore below the detection threshold of SS precursors. This implies that the vertical flow associated with the mantle plume beneath Hawaiian hotspot has not produced strong azimuthal anisotropy in the MTZ.

ACKNOWLEDGEMENTS

We thank the editor, Dr Ana Ferreira and Dr Maria Koroni as well as two anonymous reviewers for their constructive suggestions that helped improve the manuscript significantly. We also thank the developers of SPECFEM3D for distributing the codes freely online. We appreciate the help from Jeroen Ritsema, Min Chen and Kai Tao for providing their tomography models. We thank Vedran Lekic´, Jin Zhang and Wenyi Zhou for their helpful discussions about the interpretations. QH and NS were supported by the National Science Foundation (NSF) under grant NO. EAR-1447041. CB was supported by NSF under grant NO. EAR-1446978. LW is the recipient of a Discovery Early Career Research Award (project number DE170100329) funded by the Australian Government and supported by NSF under grant NO. EAR-1661985 and EAR-1853662. LW also acknowledges the Australian National University as a host institution for part of the work. RM was supported by NSF EAR Postdoctoral Fellowship 1806412.

CONFLICTS OF INTEREST

The authors declare that they have no conflicts of interest.

DATA AVAILABILITY

The SS data set was downloaded from Incorporated Research Institutions for Seismology, Data Management Center (IRIS DMC). The SS data set and MTZ topography model are available in Digital Repository at the University of Maryland (DRUM) at https://doi.org/10.13016/3ecr-1hsu.

REFERENCES

Anderson, D.L., 1962. Love wave dispersion in heterogeneous anisotropic media, *Geophysics,* **27,** 445–454.

Auer, L., Boschi, L., Becker, T.W., Nissen-Meyer, T. & Giardini, D., 2014. Savani: a variable resolution whole-mantle model of anisotropic shear velocity variations based on multiple data sets, *J. geophys. Res.,* **119,** 3006–3034.

Bai, L., Zhang, Y. & Ritsema, J., 2012. An analysis of SS precursors using spectral-element method seismograms, *Geophys. J. Int.,* **188,** 293–300.

Ballmer, M.D., Schmerr, N.C., Nakagawa, T. & Ritsema, J., 2015. Compositional mantle layering revealed by slab stagnation at ∼1000-km depth, *Sci. Adv.,* **1,** e1500815, doi:10.1126/SCIADV.1500815.

Bass, J.D. & Kanzaki, M., 1990. Elasticity of a Majorite-Pyrope solid solution, *Geophys. Res. Lett.,* **17,** 1989–1992.

Bassin, C., Laske, G. & Masters, G., 2000. The current limits of resolution for surface wave tomography in North America, *EOS, Trans. Am. Geophys. Un.,* **81,** F897.

Becker, T.W., 2006. On the effect of temperature and strain-rate dependent viscosity on global mantle flow, net rotation, and plate-driving forces, *Geophys. J. Int.,* **167,** 943–957.

Beghein, C., Resovsky, J. & Hilst, R.D. van der., 2008. The signal of mantle anisotropy in the coupling of normal modes, *Geophys. J. Int.,* **175,** 1209–1234.

Bercovici, D. & Karato, S.I., 2003. Whole-mantle convection and the transition-zone water filter, *Nature,* **425,** 39–44.

Bina, C.R. & Helffrich, G., 1994. Phase transition Clapeyron slopes and transition zone seismic discontinuity topography, *J. geophys. Res.,* **99,** 15 853–15 860.

Chang, S.J., Ferreira, A.M.G., Ritsema, J., Heijst, H.J. van & Woodhouse, J.H., 2014. Global radially anisotropic mantle structure from multiple datasets: a review, current challenges, and outlook, *Tectonophysics,* **617,** 1–19.

Chang, S.J., Ferreira, A.M.G., Ritsema, J., Heijst, H.J. van & Woodhouse, J.H., 2015. Joint inversion for global isotropic and radially anisotropic mantle structure including crustal thickness perturbations, *J. geophys. Res.,* **120,** 4278–4300.

Chen, M., Niu, F., Liu, Q., Tromp, J. & Zheng, X., 2015. Multiparameter adjoint tomography of the crust and upper mantle beneath East Asia: 1. Model construction and comparisons, *J. geophys. Res.,* **120,** 1762–1786.

Chen, W.P. & Brudzinski, M.R., 2003. Seismic anisotropy in the mantle transition zone beneath Fiji-Tonga, *Geophys. Res. Lett.,* **30**(13), doi:10.1029/2002GL016330.

Collins, J.A., Wolfe, C.J. & Laske, G., 2012. Shear wave splitting at the Hawaiian hot spot from the PLUME land and ocean bottom seismometer deployments, *Geochem. Geophys. Geosyst.,* **13,** doi:10.1029/2011GC003881.

Cordier, A.P., Mainprice, A.D. & Mosenfelder, J.L., 2004. Mechanical instability near the stishovite-$CaCl_2$ phase transition: implications for crystal preferred orientations and seismic properties, *Eur. J. Mineral.,* **16,** 387–399.

Crampin, S., 1984. An introduction to wave propagation in anisotropic media, *Geophys. J. R. astr. Soc.,* **76,** 17–28.

Dahlen, F.A., 2005. Finite-frequency sensitivity kernels for boundary topography perturbations, *Geophys. J. Int.,* **162,** 525–540.

Debayle, E., Dubuffet, F. & Durand, S., 2016. An automatically updated S-wave model of the upper mantle and the depth extent of azimuthal anisotropy, *Geophys. Res. Lett.,* **43,** 674–682.

DeMets, C., Gordon, R.G., Argus, D.F. & Stein, S., 1990. Current plate motions, *Geophys. J. Int.,* **101,** 425–478.

Demouchy, S., Mainprice, D., Tommasi, A., Couvy, H., Barou, F., Frost, D.J. & Cordier, P., 2011. Forsterite to wadsleyite phase transformation under shear stress and consequences for the Earth's mantle transition zone, *Phys. Earth planet. Inter.,* **184,** 91–104.

Deuss, A. & Woodhouse, J.H., 2002. A systematic search for mantle discontinuities using SS-precursors, *Geophys. Res. Lett.,* **29,** 90–94.

Dziewonski, A.M. & Anderson, D.L., 1981. Preliminary reference Earth model, *Phys. Earth planet. Inter.,* **25,** 297–356.

Efron, B. & Tibshirani, R., 1986. Bootstrap methods for standard errors, confidence intervals, and other measures of statistical accuracy, *Stat. Sci.,* **1,** 54–75.

Faccenda, M., 2014. Mid mantle seismic anisotropy around subduction zones, *Phys. Earth planet. Inter.,* **227,** 1–19, Elsevier.

Faccenda, M. & Capitanio, F.A., 2012. Development of mantle seismic anisotropy during subduction-induced 3-D flow, *Geophys. Res. Lett.,* **39**(11), doi:10.1029/2012GL051988.

Faccenda, M., Ferreira, A.M.G., Tisato, N., Lithgow-Bertelloni, C., Stixrude, L. & Pennacchioni, G., 2019. Extrinsic elastic anisotropy in a compositionally heterogeneous Earth's mantle, *J. geophys. Res.,* **124,** 1671–1687.

Ferreira, A.M.G., Faccenda, M., Sturgeon, W., Chang, S.J. & Schardong, L., 2019. Ubiquitous lower-mantle anisotropy beneath subduction zones, *Nat. Geosci.,* **12,** 301–306.

Flanagan, M.P. & Shearer, P.M., 1998. Global mapping of topography on transition zone velocity discontinuities by stacking *SS* precursors, *J. geophys. Res.,* **103,** 2673–2692.

Foley, B.J. & Long, M.D., 2011. Upper and mid-mantle anisotropy beneath the Tonga slab, *Geophys. Res. Lett.,* **38,** L02303, doi:10.1029/2010GL046021.

Fouch, M.J. & Fischer, K.M., 1996. Mantle anisotropy beneath northwest Pacific subduction zones, *J. geophys. Res.,* **101,** 15 987–16 002.

Friederich, W. & Dalkolmo, J., 1995. Complete synthetic seismograms for a spherically symmetric earth by a numerical computation of the Green's function in the frequency domain, *Geophys. J. Int.,* **122,** 537–550.

Fukao, Y. & Obayashi, M., 2013. Subducted slabs stagnant above, penetrating through, and trapped below the 660 km discontinuity, *J. geophys. Res.,* **118,** 5920–5938.

Gu, Y.J. & Dziewonski, A.M., 2002. Global variability of transition zone thickness, *J. geophys. Res.,* **107,** ESE 2–1-ESE 2-17.

Guo, Z. & Zhou, Y., 2020. Finite-frequency imaging of the global 410- and 660-km discontinuities using SS precursors, *Geophys. J. Int.,* **220,** 1978–1994.

Gung, Y., Panning, M. & Romanowicz, B., 2003. Global anisotropy and the thickness of continents, *Nature,* **422,** 707–711.

Hao, S., Wang, W., Qian, W. & Wu, Z., 2019. Elasticity of akimotoite under the mantle conditions: implications for multiple discontinuities and seismic anisotropies at the depth of -600–750 km in subduction zones, *Earth planet. Sci. Lett.,* **528,** doi:10.1016/j.epsl.2019.115830.

Hayes, G.P., Wald, D.J. & Johnson, R.L., 2012. Slab1.0: a three-dimensional model of global subduction zone geometries, *J. geophys. Res.,* **117**(B1), doi:10.1029/2011JB008524.

Helffrich, G., 2000. Topography of the transition zone seismic discontinuities, *Rev. Geophys.,* **38,** 141–158.

Houser, C., Masters, G., Flanagan, M. & Shearer, P., 2008. Determination and analysis of long-wavelength transition zone structure using SS precursors, *Geophys. J. Int.,* **174,** 178–194.

Huang, J. & Zhao, D., 2006. High-resolution mantle tomography of China and surrounding regions, *J. geophys. Res.,* **111,** doi:10.1029/2005JB004066.

Huang, Q., Schmerr, N., Waszek, L. & Beghein, C., 2019. Constraints on seismic anisotropy in the mantle transition zone from long-period SS precursors, *J. geophys. Res.,* **124,** 6779–6800.

Ishii, T., Kojitani, H. & Akaogi, M., 2019. Phase relations of Harzburgite and MORB up to the uppermost lower mantle conditions: precise comparison with Pyrolite by multisample cell high-pressure experiments with implication to dynamics of subducted slabs, *J. geophys. Res.,* **124,** 3491–3507.

Ita, J. & Stixrude, L., 1992. Petrology, elasticity, and composition of the mantle transition zone, *J. geophys. Res.,* **97,** 6849–6866.

Ito, E. & Takahashi, E., 1989. Postspinel transformations in the system Mg_2SiO_4-Fe_2SiO_4 and some geophysical implications, *J. geophys. Res.,* **94,** 10 637–10 646.

Jiang, F., Gwanmesia, G.D., Dyuzheva, T.I. & Duffy, T.S., 2009. Elasticity of stishovite and acoustic mode softening under high pressure by Brillouin scattering, *Phys. Earth planet. Inter.,* **172,** 235–240.

Jung, H. & Karato, S.I., 2001. Water-induced fabric transitions in olivine, *Science,* **293,** 1460–1463.

Karato, S.I., Jung, H., Katayama, I. & Skemer, P., 2008. Geodynamic significance of seismic anisotropy of the upper mantle: new insights from laboratory studies, *Annu. Rev. Earth planet. Sci.,* **36,** 59–95.

Katsura, T. & Ito, E., 1989. The system Mg_2SiO_4-Fe_2SiO_4 at high pressures and temperatures: precise determination of stabilities of olivine, modified spinel, and spinel, *J. geophys. Res.,* **94,** 15 663–15 670.

Kawakatsu, H., Kumar, P., Takei, Y., Shinohara, M., Kanazawa, T., Araki, E. & Suyehiro, K., 2009. Seismic evidence for sharp lithosphere-asthenosphere boundaries of oceanic plates, *Science,* **324,** 499–502.

Kawakatsu, H. & Yoshioka, S., 2011. Metastable olivine wedge and deep dry cold slab beneath southwest Japan, *Earth planet. Sci. Lett.,* **303,** 1–10.

Kawazoe, T., Ohuchi, T., Nishihara, Y., Nishiyama, N., Fujino, K. & Irifune, T., 2013. Seismic anisotropy in the mantle transition zone induced by shear deformation of wadsleyite, *Phys. Earth planet. Inter.,* **216,** 91–98

Kiefer, B., Stixrude, L. & Wentzcovitch, R.M., 1997. Calculated elastic constants and anisotropy of Mg2SiO4 spinel at high pressure, *Geophys. Res. Lett.,* **24,** 2841–2844.

Komatitsch, D. & Tromp, J., 2002. Spectral-element simulations of global seismic wave propagation - II. Three-dimensional models, oceans, rotation and self-gravitation, *Geophys. J. Int.,* **150,** 303–318.

Komatitsch, D. & Tromp, J., 2002. Spectral-element simulations of global seismic wave propagation - I. Validation, *Geophys. J. Int.,* **149,** 390–412.

Koroni, M. & Trampert, J., 2016. The effect of topography of upper-mantle discontinuities on SS precursors, *Geophys. J. Int.,* **204,** 667–681.

Lawrence, J.F. & Shearer, P.M., 2008. Imaging mantle transition zone thickness with SdS-SS finite-frequency sensitivity kernels, *Geophys. J. Int.,* **174,** 143–158.

Leo, J.F., Wookey, J., Hammond, J.O.S., Kendall, J.M., Kaneshima, S., Inoue, H., Yamashina, T. *et al.*, 2012. Mantle flow in regions of complex tectonics: insights from Indonesia, *Geochem. Geophys. Geosyst.,* **13,** 253, doi:10.1029/2012GC004417.

Li, J., Zheng, Y., Thomsen, L., Lapen, T.J. & Fang, X., 2018. Deep earthquakes in subducting slabs hosted in highly anisotropic rock fabric, *Nat. Geosci.,* **11,** 696–700.

Li, L., Weidner, D.J., Brodholt, J., Alfè, D. & Price, G.D., 2006. Elasticity of Mg_2SiO_4 ringwoodite at mantle conditions, *Phys. Earth planet. Inter.,* **157,** 181–187.

Long, M.D. & Hilst, R.D. van der., 2005. Upper mantle anisotropy beneath Japan from shear wave splitting, *Phys. Earth planet. Inter.,* **151,** 206–222.

Lynner, C. & Long, M.D., 2015. Heterogeneous seismic anisotropy in the transition zone and uppermost lower mantle: evidence from South America, Izu-Bonin and Japan, *Geophys. J. Int.,* **201,** 1545–1552.

Mainprice, D., Tommasi, A., Couvy, H., Cordier, P. & Frost, D.J., 2005. Pressure sensitivity of olivine slip systems and seismic anisotropy of Earth's upper mantle, *Nature,* **433,** 731–733.

Marone, F. & Romanowicz, B., 2007. The depth distribution of azimuthal anisotropy in the continental upper mantle, *Nature,* **447,** 198–201.

Mohiuddin, A., Long, M.D. & Lynner, C., 2015. Mid-mantle seismic anisotropy beneath southwestern Pacific subduction systems and implications for mid-mantle deformation, *Phys. Earth planet. Inter.,* **245,** 1–14.

Mondal, P. & Long, M.D., 2020. Strong seismic anisotropy in the deep upper mantle beneath the Cascadia backarc: constraints from probabilistic finite-frequency SKS splitting intensity tomography, *Earth planet. Sci. Lett.,* **539,** doi:10.1016/j.epsl.2020.116172.

Montagner, J. P. & Nataf, H.C., 1986. A simple method for inverting the azimuthal anisotropy of surface waves, *J. geophys. Res.,* **91,** 511–520.

Montagner, Jean Paul, Griot-Pommera, D.A. & Lavé, J., 2000. How to relate body wave and surface wave anisotropy? *J. geophys. Res.,* **105,** 19 015–19 027.

Moulik, P. & Ekström, G., 2014. An anisotropic shear velocity model of the Earth's mantle using normal modes, body waves, surface waves and long-period waveforms, *Geophys. J. Int.,* **199,** 1713–1738.

Nettles, M. & Dziewoński, A.M., 2008. Radially anisotropic shear velocity structure of the upper mantle globally and beneath North America, *J. geophys. Res.,* **113,** 219.

Nowacki, A., Kendall, J.M., Wookey, J. & Pemberton, A., 2015. Mid-mantle anisotropy in subduction zones and deep water transport, *Geochem. Geophys. Geosyst.,* **16,** 764–784.

Ohuchi, T., Fujino, K., Kawazoe, T. & Irifune, T., 2014. Crystallographic preferred orientation of wadsleyite and ringwoodite: effects of phase transformation and water on seismic anisotropy in the mantle transition zone, *Earth planet. Sci. Lett.,* **397,** 133–144.

Pamato, M.G. *et al.*, 2016. Single crystal elasticity of majoritic garnets: stagnant slabs and thermal anomalies at the base of the transition zone, *Earth planet. Sci. Lett.,* **451,** 114–124.

Peterson, J.R., 1993. Observations and modeling of seismic background noise, Open-File Report, doi:10.3133/OFR93322.

Phipps Morgan, J. & Shearer, P.M., 1993. Seismic constraints on mantle flow and topography of the whole mantle convection, *Nature,* **365,** 506–511.

Ringwood, A.E., 1975. *Composition and Petrology of the Earth'S Mantle,* McGraw-Hill.

Ritsema, J., Deuss, A., Heijst, H.J. van & Woodhouse, J.H., 2011. S40RTS: a degree-40 shear-velocity model for the mantle from new Rayleigh wave dispersion, teleseismic traveltime and normal-mode splitting function measurements, *Geophys. J. Int.,* **184,** 1223–1236.

Rychert, C.A., Harmon, N. & Schmerr, N., 2014. Synthetic waveform modelling of SS precursors from anisotropic upper-mantle discontinuities, *Geophys. J. Int.,* **196,** 1694–1705.

Rychert, C.A., Schmerr, N. & Harmon, N., 2012. The Pacific lithosphere-asthenosphere boundary: seismic imaging and anisotropic constraints from SS waveforms, *Geochem. Geophys. Geosyst.,* **13,** doi:10.1029/2012gc004194.

Saki, M., Thomas, C., Merkel, S. & Wookey, J., 2018. Detecting seismic anisotropy above the 410 km discontinuity using reflection coefficients of underside reflections, *Phys. Earth planet. Inter.,* **274,** 170–183.

Sang, L. & Bass, J.D., 2014. Single-crystal elasticity of diopside to 14GPa by Brillouin scattering, *Phys. Earth planet. Inter.,* **228,** 75–79.

Sawamoto, H., Weidner, D.J., Sasaki, S. & Kumazawa, M., 1984. Single-crystal elastic properties of the modified spinel (beta) phase of magnesium orthosilicate, *Science,* **224,** 749–751.

Schaeffer, A.J., Lebedev, S. & Becker, T.W., 2016. Azimuthal seismic anisotropy in the Earth's upper mantle and the thickness of tectonic plates, *Geophys. J. Int.,* **207,** 901–933.

Schmerr, N. & Garnero, E., 2006. Investigation of upper mantle discontinuity structure beneath the central Pacific using SS precursors, *J. geophys. Res.,* **111**(B8), doi:10.1029/2005JB004197.

Schmerr, N., Garnero, E. & McNamara, A., 2010. Deep mantle plumes and convective upwelling beneath the Pacific Ocean, *Earth planet. Sci. Lett.,* **294,** 143–151.

Sharp, T.G., Bussod, G.Y.A. & Katsura, T., 1994. , *Phys. Earth planet. Inter.,* **86,** 69–83.

Shiraishi, R., Ohtani, E., Kanagawa, K., Shimojuku, A. & Zhao, D., 2008. Crystallographic preferred orientation of akimotoite and seismic anisotropy of Tonga slab, *Nature,* **455,** 657–660.

Silver, P.G. & Chan, W.W., 1988. Implications for continental structure and evolution from seismic anisotropy, *Nature,* **335,** 34–39.

Sinogeikin, S. V., Katsura, T. & Bass, J.D., 1998. Sound velocities and elastic properties of Fe-bearing wadsleyite and ringwoodite, *J. geophys. Res.,* **103,** 20 819–20 825.

Sinogeikin, S.V., Bass, J.D. & Katsura, T., 2003. Single-crystal elasticity of ringwoodite to high pressures and high temperatures: implications for 520 km seismic discontinuity, *Phys. Earth planet. Inter.,* **136,** 41–66.

Stixrude, L., 1997. Structure and sharpness of phase transitions and mantle discontinuities, *J. geophys. Res.,* **102,** 14 835–14 852.

Sturgeon, W., Ferreira, A.M.G., Faccenda, M., Chang, S.J. & Schardong, L., 2019. On the origin of radial anisotropy near subducted slabs in the midmantle, *Geochem. Geophys. Geosyst.,* **20,** 5105–5125.

Tao, K., Grand, S.P. & Niu, F., 2018. Seismic structure of the upper mantle beneath eastern Asia from full waveform seismic tomography, *Geochem. Geophys. Geosyst.,* **19,** 2732–2763.

Thomas, C. & Billen, M.I., 2009. Mantle transition zone structure along a profile in the SW Pacific: thermal and compositional variations, *Geophys. J. Int.,* **176,** 113–125.

Thurel, E. & Cordier, P., 2003. Plastic deformation of wadsleyite: I. High-pressure deformation in compression, *Phys. Chem. Miner.,* **30,** 256–266.

Tian, Y., Zhu, H., Zhao, D., Liu, C., Feng, X., Liu, T. & Ma, J., 2016. Mantle transition zone structure beneath the Changbai volcano: insight into deep slab dehydration and hot upwelling near the 410 km discontinuity, *J. geophys. Res.,* **121,** 5794–5808.

Tommasi, A., Mainprice, D., Cordier, P., Thoraval, C. & Couvy, H., 2004. Strain-induced seismic anisotropy of wadsleyite polycrystals and flow patterns in the mantle transition zone, *J. geophys. Res.,* **109,** 1–10.

Tong, C., Gudmundsson, O. & Kennett, B.L.N., 1994. Shear wave splitting in refracted waves returned from the upper mantle transition zone beneath northern Australia, *J. geophys. Res.,* **99,** 15 783–15 797.

Trampert, J. & Heijst, H.J. van., 2002. Global azimuthal anisotropy in the transition zone, *Science,* **296,** 1297–1299.

Visser, K., Trampert, J. & Kennett, B.L.N., 2008. Global anisotropic phase velocity maps for higher mode Love and Rayleigh waves, *Geophys. J. Int.,* **172,** 1016–1032.

Waszek, L., Schmerr, N.C. & Ballmer, M.D., 2018. Global observations of reflectors in the mid-mantle with implications for mantle structure and dynamics, *Nat. Commun.,* **9,** 385, doi:10.1038/s41467-017-02709-4.

Wei, W., Zhao, D., Xu, J., Wei, F. & Liu, G., 2015. P and S wave tomography and anisotropy in Northwest Pacific and East Asia: constraints on stagnant slab and intraplate volcanism, *J. geophys. Res.,* **120,** 1642–1666.

Weidner, D.J., Sawamoto, H. & Sasaki, S., 1984. Single-crystal elastic properties of the spinel phase of Mg_2SiO_4, *J. geophys. Res.,* **89,** 7852–7860.

Wirth, E.A. & Long, M.D., 2014. A contrast in anisotropy across mid-lithospheric discontinuities beneath the central United States—a relic of craton formation, *Geology,* **42,** 851–854.

Wolfe, C.J. & Silver, P.G., 1998. Seismic anisotropy of oceanic upper mantle: shear wave splitting methodologies and observations, *J. geophys. Res.,* **103,** 749–771.

Xu, F., Yamazaki, D., Tsujino, N. & Guan, L., 2020. Lattice preferred orientation of stishovite deformed at high pressure and high temperature, *Phys. Earth planet. Inter.,* **306,** doi:10.1016/j.pepi.2020.106546.

Yan, J., Ballmer, M.D. & Tackley, P.J., 2020. The evolution and distribution of recycled oceanic crust in the Earth's mantle: insight from geodynamic models, *Earth planet. Sci. Lett.,* **537,** doi:10.1016/j.epsl.2020.116171.

Yang, J., Mao, Z., Lin, J.F. & Prakapenka, V.B., 2014. Single-crystal elasticity of the deep-mantle magnesite at high pressure and temperature, *Earth planet. Sci. Lett.,* **392,** 292–299.

Yu, C., Day, E.A., Hoop, M. v. de, Campillo, M. & Hilst, R.D. van der., 2017. Mapping mantle transition zone discontinuities beneath the central pacific with array processing of SS precursors, *J. geophys. Res.,* **122,** 10 364–10 378.

Yuan, K. & Beghein, C., 2018. A Bayesian method to quantify azimuthal anisotropy model uncertainties: application to global azimuthal anisotropy in the upper mantle and transition zone, *Geophys. J. Int.,* **213,** 603–622.

Yuan, K. & Beghein, C., 2013. Seismic anisotropy changes across upper mantle phase transitions, *Earth planet. Sci. Lett.,* **374,** 132–144, Elsevier.

Yuan, K. & Beghein, C., 2014. Three-dimensional variations in Love and Rayleigh wave azimuthal anisotropy for the upper 800 km of the mantle, *J. geophys. Res.,* **119,** 3232–3255.

Zha, C.S., Duffy, T.S., Mao, H.K., Downs, R.T., Hemley, R.J. & Weidner, D.J., 1997. Single-crystal elasticity of β-Mg_2SiO_4 to the pressure of the 410 km seismic discontinuity in the Earth's mantle, *Earth planet. Sci. Lett.,* **147,** E9–E15.

Zhang, H., Schmandt, B. & Zhang, J.S., 2021. Localized anisotropy in the mantle transition zone due to flow through slab gaps, *Geophys. Res. Lett.,* **48,** doi:10.1029/2021GL092712.

Zhang, J.S., Bass, J.D. & Schmandt, B., 2018. The elastic anisotropy change near the 410-km discontinuity: predictions from single-crystal elasticity measurements of olivine and wadsleyite, *J. geophys. Res.,* **123,** 2674–2684.

Zhang, J.S., Hao, M., Ren, Z. & Chen, B., 2019. The extreme acoustic anisotropy and fast sound velocities of cubic high-pressure ice polymorphs at Mbar pressure, *Appl. Phys. Lett.,* **114,** doi:10.1063/1.5096989.

Zhao, D., Tian, Y., Lei, J., Liu, L. & Zheng, S., 2009. Seismic image and origin of the Changbai intraplate volcano in East Asia: role of big mantle wedge above the stagnant Pacific slab, *Phys. Earth planet. Inter.,* **173,** 197–206.

Zhao, L. & Chevrot, S., 2003. SS-wave sensitivity to upper mantle structure: implications for the mapping of transition zone discontinuity topographies, *Geophys. Res. Lett.,* **30,** doi:10.1029/2003GL017223.

Zhou, W.Y. *et al.*, 2021. The water-Fe-pressure dependent single-crystal elastic properties of wadsleyite: implications for the seismic anisotropy in the upper Mantle Transition Zone, *Earth planet. Sci. Lett.,* **565,** doi:10.1016/j.epsl.2021.116955.

SUPPORTING INFORMATION

Supplementary data are available at *GJI* online.

Figure S1. (a) Same as Fig. 4 but for the model with two layers of anisotropy: first layer in shallow upper mantle (80–220 km) and second layer in the MTZ (400–670 km). The light green bars represent the LPO of olivine with fast axis Θ_1. The dark green and blue bars denote the LPO of wadsleyite and ringwoodite, respectively. These two minerals have the same fast axis Θ_2. The measurements of (b) S410S−SS time residuals, (c) S660S−SS time residuals, (d) S660S−S410S time residuals, (e) S410S/SS and S660S/SS amplitudes from the azimuthal stacking of SPECFEM3D synthetics are shown as a function of bounce point azimuths.

Figure S2. (a) Same as Fig. 4 but for the model with two sublayers of anisotropy in the upper MTZ (400–520 km) and lower MTZ (520–670 km). The green bars represent the LPO of wadsleyite with fast axis Θ_1, and the blue bars represent the LPO of ringwoodite with fast axis Θ_2. The measurements of (b) S410S−SS time residuals, (c) S660S−SS time residuals, (d) S660S−S410S time residuals, (e) S410S/SS and S660S/SS amplitudes from the azimuthal stacking of SPECFEM3D synthetics are shown as a function of bounce point azimuths.

Figure S3. Same as Fig. 10 but using a realistic source–receiver geometry. The dlnG detectability matrix for (a) S660S−S410S time, (b) S660S−SS time, (c) S410S/SS amplitude and (d) S660S/SS amplitude.

Figure S4. Comparisons between a global tomography model S40RTS (Ritsema *et al*. 2011) and two regional tomography models: EARA2014 (Chen *et al*. 2015) and FWEA18 (Tao *et al*. 2018) in the upper mantle. The magenta box highlights our study region in the Japan subduction zone. The regional models can better image the shape of subducting slab as well as the low V_S anomalies in the upper mantle.

Figure S5. Same as Fig. S4 but for the MTZ depth (410–660 km). In the MTZ, S40RTS underestimates the V_S anomalies associated with stagnant slab compared to the two regional models.

Figure S6. Comparisons of S660S−S410S time residuals and MTZ anisotropy inversions in the Japan subduction zone after tomography corrections using three different models: (a) S40RTS (Ritsema *et al*. 2011), (b) EARA2014 (Chen *et al*. 2015) and (c) FWEA18 (Tao *et al*. 2018). The grid-search results of the best-fitting models and error ellipses are shown in bottom panels (d), (e) and (f) for S40RTS, EARA2014 and FWEA18, respectively. The legends are the same as Fig. 12.

Figure S7. Comparisons of S410S/SS amplitudes and MTZ anisotropy inversions in the Japan subduction zone after tomography corrections using three different models: (a) S40RTS (Ritsema *et al*. 2011), (b) EARA2014 (Chen *et al*. 2015) and (c) FWEA18 (Tao *et al*. 2018). The grid-search results of the best-fitting models and error ellipses are shown in bottom panels (d), (e) and (f) for S40RTS, EARA2014 and FWEA18, respectively. The legends are the same as Fig. 12.